

AD-A036 141

DAYTON UNIV OHIO RESEARCH INST  
WATER DROP/BOW SHOCK INTERACTIONS. (U)

F/G 20/4

UNCLASSIFIED

JUN 75 J P BARBER, E S GROOM, H R TAYLOR

F33615-73-C-5027

AFML-TR-75-105

NL

1 OF 1  
AD  
A036141







ADA036141

AFML-TR-75-105

2  
B.S.

## WATER DROP/BOW SHOCK INTERACTIONS

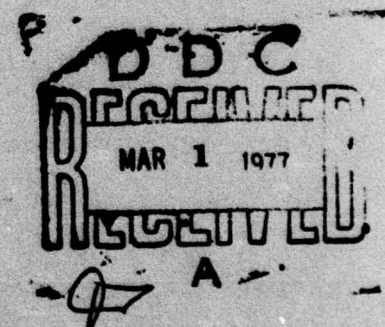
University of Dayton Research Institute ✓

and

Air Force Materials Laboratory

TECHNICAL REPORT AFML-TR-75-105

JUNE 1975



Approved for public release; distribution unlimited.

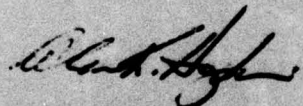
AIR FORCE MATERIALS LABORATORY  
AIR FORCE SYSTEMS COMMAND  
WRIGHT-PATTERSON AIR FORCE BASE, OHIO

# NOTICE

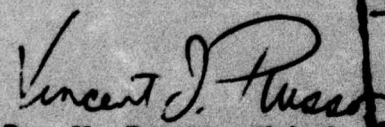
When Government drawings, specifications, or other data are used for any purpose other than in connection with a definitely related Government procurement operation, the United States Government thereby incurs no responsibility nor any obligation whatsoever; and the fact that the government may have formulated, furnished, or in any way supplied the said drawings, specifications, or other data, is not to be regarded by implication or otherwise as in any manner licensing the holder or any other person or corporation, or conveying any rights or permission to manufacture, use, or sell any patented invention that may in any way be related thereto.

This report has been reviewed and cleared for open publication and/or public release by the appropriate Office of Information (OI) in accordance with AFR 190-170 and DODD 5230.9. There is no objection to unlimited distribution of this report to the public at large or by DDC to the National Technical Information Service (NTIS).

This technical report has been reviewed and is approved for publication.

  
A.K. HOPKINS  
Project Engineer

FOR THE COMMANDER

  
Dr. V. Russo, Chief  
Metals Behavior Branch  
Metals & Ceramics Division  
Air Force Materials Laboratory

APPROVED FOR	
OTIS	<input checked="" type="checkbox"/>
DD	<input checked="" type="checkbox"/>
CHANGES	<input type="checkbox"/>
JUSTIFICATION	<input type="checkbox"/>
BY	
DATE	
REMARKS	

Copies of this report should not be returned unless return is required by security considerations, contractual obligations, or notice on a specific document.



UNCLASSIFIED

SECURITY CLASSIFICATION OF THIS PAGE (When Data Entered)

REPORT DOCUMENTATION PAGE		READ INSTRUCTIONS BEFORE COMPLETING FORM
1. REPORT NUMBER <b>AFML-TR-75-105</b>	2. GOVT ACCESSION NO.	3. RECIPIENT'S CATALOG NUMBER
4. TITLE (and Subtitle) <b>WATER DROP/BOW SHOCK INTERACTIONS.</b>		5. TYPE OF REPORT & PERIOD COVERED <b>Progress Report,</b>
7. AUTHOR(s) <b>John P. Barber, Henry R. Taylor Edward S. Grood, Alan K. Hopkins</b>		6. PERFORMING ORG. REPORT NUMBER <b>F33615-73-C-5027</b>
9. PERFORMING ORGANIZATION NAME AND ADDRESS <b>The University of Dayton 300 College Park Dayton, Ohio 45469</b>		10. PROGRAM ELEMENT, PROJECT, TASK AREA & WORK UNIT NUMBERS <b>7351, 735106, 73510689</b>
11. CONTROLLING OFFICE NAME AND ADDRESS <b>Air Force Materials Lab Wright-Patterson Air Force Base Dayton, Ohio</b>		12. REPORT DATE <b>Jun 75</b>
14. MONITORING AGENCY NAME & ADDRESS (if different from Controlling Office) <b>As above</b>		13. NUMBER OF PAGES <b>77</b>
		15. SECURITY CLASS. (of this report) <b>UNCLASSIFIED</b>
		15a. DECLASSIFICATION/DOWNGRADING SCHEDULE
16. DISTRIBUTION STATEMENT (of this Report) <b>Approved for public release; distribution unlimited.</b>		
17. DISTRIBUTION STATEMENT (of the abstract entered in Block 20, if different from Report) <b>Approved for public release; distribution unlimited.</b>		
18. SUPPLEMENTARY NOTES		
19. KEY WORDS (Continue on reverse side if necessary and identify by block number) <b>Rain erosion, water droplet, laser camera, bow shocks</b>		
20. ABSTRACT (Continue on reverse side if necessary and identify by block number) <b>The interaction of water drops of diameters in the range of 20 to 200 <math>\mu</math>m with reentry vehicle bow shocks was investigated with a microscope/Q-spoiled laser camera system. A single stream of water drops was generated on the trajectory of a Mach 12 projectile launched from a light gas gun. The microscope/Q-spoiled laser camera was used to obtain high resolution photographs of the nose tip region of the projectile as it encountered the water droplets. <math>\rightarrow</math> next page</b>		

DD FORM 1 JAN 75 1473

EDITION OF 1 NOV 68 IS OBSOLETE

UNCLASSIFIED

SECURITY CLASSIFICATION OF THIS PAGE (When Data Entered)

105400

**UNCLASSIFIED**

SECURITY CLASSIFICATION OF THIS PAGE(When Data Entered)

→ An analytic study of the droplet/bow shock interaction was undertaken. Calculations showed that droplets above about 20 <sup>micrometers</sup>  $\mu\text{m}$  in diameter should remain intact and impact the projectile nose tip in the stagnation region. In the stagnation region droplets of this size should experience little deviation from a straight trajectory (i. e., no sweeping action would be expected).

These predictions were confirmed experimentally using the techniques described in this report.

**UNCLASSIFIED**

SECURITY CLASSIFICATION OF THIS PAGE(When Data Entered)



**AFML-TR-75-105**

**WATER DROP/BOW SHOCK INTERACTIONS**

**Dr. John P. Barber  
Dr. Edward S. Grood  
Mr. Henry R. Taylor**

**University of Dayton Research Institute**

**and**

**Dr. Alan K. Hopkins  
Air Force Materials Laboratory**

**TECHNICAL REPORT AFML-TR-75-105**

**JUNE 1975**

**Approved for public release; distribution unlimited.**

**AIR FORCE MATERIALS LABORATORY  
AIR FORCE SYSTEMS COMMAND  
WRIGHT-PATTERSON AIR FORCE BASE, OHIO**

## FOREWORD

The program described in this report was carried out by the University of Dayton at the Air Force Materials Laboratories, Wright-Patterson Air Force Base, Dayton, Ohio, under contract F33615-73-C-5027.

The work was conducted during the period January, 1974, to November, 1974, and was monitored by Dr. Alan K. Hopkins of the Air Force Materials Laboratory.

This report was submitted by the authors in March, 1975, for publication as an AFML Technical Report. The work was performed under Project 7351 Metallic Materials, Task 735106 Behavior of Metals Used in Flight Vehicle and Engine Structural Applications.



## TABLE OF CONTENTS

SECTION	PAGE
1 INTRODUCTION	1
2 EXPERIMENTAL TECHNIQUES AND DEVELOPMENT	2
2.1 General Description of Light Gas Gun	2
2.2 Image Converter Camera Systems	4
2.3 Q-spoil Laser/Microscope Camera Photographic System	10
2.4 Triggering Techniques	15
2.5 Water Drop Generator	16
3 ANALYTIC INVESTIGATION	19
3.1 Introduction/Objective	19
3.2 Experimental Studies	20
3.3 Physical Process	23
3.4 Shock Standoff Distance	30
3.5 Effect of Mach Number on Stripping	30
3.6 Trajectory Studies	34
4 EXPERIMENTAL RESULTS	39
4.1 Image Converter Photographs	39
4.2 Microscope Camera Photographs	41
5 CONCLUSIONS	44
APPENDIX A: IMAGE CONVERTER CAMERA SYSTEM PHOTOGRAPHS	
APPENDIX B: MICROSCOPE/LASER CAMERA SYSTEM PHOTOGRAPHS; HIGH VELOCITY ENCOUNTERS	
APPENDIX C: MICROSCOPE/LASER CAMERA SYSTEM PHOTOGRAPHS; LOW VELOCITY ENCOUNTERS	
REFERENCES	

# LIST OF ILLUSTRATIONS

FIGURE		PAGE
1.	A schematic of the range used for erosion studies.	3
2.	Typical projectiles used in the water drop/bow shock interaction investigation.	4
3.	Single image converter camera shadowgraph system.	5
4.	A single image converter camera photograph showing small drops traversing the bow shock.	6
5.	A single image converter camera picture showing impact debris plumes.	6
6.	Four image converter camera system arrangement.	8
7.	A typical four image converter camera system sequence.	9
8.	A schematic of the optics of the microscope/laser camera system.	11
9.	The Q-spoiled laser.	12
10.	A schematic of the microscope/Q-spoiled laser camera system.	12
11.	A photograph of the microscope/Q-spoiled laser camera system on the range.	13
12.	A photograph of water drop/bow shock interaction obtained with the microscope/Q-spoiled laser camera.	14
13.	A schematic of the up-down counter trigger system.	16
14.	The vibrating capillary water drop generator.	17
15.	A schematic of the water drop/bow shock interaction.	21
16.	A schematic of a water droplet in the shock front.	24
17.	Droplet Mach number as a function of vehicle Mach number.	25
18.	Pressure ratio across the shock.	26
19.	Density ratio across the shock.	27
20.	Temperature ratio across the shock.	28
21.	Shock standoff distance as a function of projectile Mach number.	29
22.	The mass fraction of droplet remaining at impact.	32



# LIST OF ILLUSTRATIONS (CONTD)

FIGURE		PAGE
23.	The droplet kinetic energy fraction remaining at impact.	33
24.	Droplet mass ratio remaining at impact as a function of initial drop size and vehicle Mach number.	34
25.	Trajectories of water drops at off axis positions.	36
26.	Mass fraction for droplets entering the shock off axis at $R = 0.3R_N$ .	37
27.	Kinetic energy fraction for droplet entering the shock off axis at $R = 0.3R_N$ .	38
28.	Image converter camera sequence.	40
29.	Microscope/laser camera picture.	42
30.	Microscope/laser camera picture.	43
31.	Microscope/laser camera picture.	44
32.	Microscope/laser camera picture.	46

## LIST OF TABLES

TABLE	PAGE
1. RANGE OF PHYSICAL CONDITIONS STUDIED	19



# LIST OF SYMBOLS

$D_o$	- initial droplet diameter	$\epsilon$	- density ratio across the shock
$D$	- droplet frontal diameter	$\sigma_d$	- droplet surface tension
$KE$	- droplet kinetic energy	$\gamma$	- ratio of specific heats for a gas
$KE_o$	- initial droplet kinetic energy	$\rho_1$	- gas density in front of the shock
$l$	- distance shock wave moves past initial droplet position	$\rho_2$	- gas density behind the shock
$m_o$	- initial droplet mass	$\rho_d$	- droplet fluid density
$m$	- droplet mass	$\Delta$	- shock stand off distance
$P_1$	- pressure in front of the shock		
$P_2$	- pressure behind the shock		
$U_s$	- shock velocity		
$U_2$	- gas velocity behind shock		
$U_d$	- droplet velocity		
$R_N$	- nose tip radius		
$S$	- distance shock moves past droplet		
$t$	- time		
$t_c$	- time for catastrophic breakup		
$t_s$	- time for complete stripping		
$T$	- non dimensional time		
$T_c$	- non dimensional time for catastrophic breakup to occur		
$T_s$	- non dimensional time for complete mass stripping		
$x$	- displacement of droplet		
$X$	- non dimensional droplet displacement		

## SECTION 1

### INTRODUCTION

Hypervelocity reentry vehicles have a high probability of encountering clouds during reentry. The impact of water droplets, which make up the cloud, on the nose cone of the reentry vehicle might result in severe and perhaps catastrophic erosion of the vehicle. The behavior of small water drops as they traverse the vehicle bow shock, travel through the shocked air and finally impact the surface is the subject of this investigation.

The report describes a high resolution, high speed camera system developed to facilitate direct observation of small drops (10  $\mu\text{m}$  to 200  $\mu\text{m}$  diameter) and their interactions with the bow shock region and the nose tips of reentry vehicle models. Also included is an analytic study of droplet/bow shock interactions and experimental observations obtained with the camera system which are in agreement with analytic predictions.



## SECTION 2

### EXPERIMENTAL TECHNIQUES AND DEVELOPMENT

#### 2.1 GENERAL DESCRIPTION OF LIGHT GAS GUN

Light gas guns are commonly used for the study of hypervelocity impact phenomena. The three basic components of a light gas gun are a pumptube in which the gas (usually  $H_2$  or He) is isentropically heated and compressed, a high pressure chamber in which the final stage of compression occurs, and a launch tube in which the projectile is accelerated.

The AFML light gas gun used in the experiments discussed in this report consists of a 40 mm bore 488 cm long pumptube, a 33 cm long high pressure section with a tapered 40 mm chamber, and a 20 mm bore 244 cm long launch tube. Valving of gas from the high pressure section to launch tube coupling is accomplished by rupturing a 1.5 mm thick aluminum disk. The muzzle end of the launch tube is coupled to a 91 cm diameter 152 cm long blast tank in which the muzzle gas expands.

It was necessary to provide a large evacuated chamber volume to prevent overpressuring the range with muzzle gas, while maintaining the desired atmospheric pressure in the "target" chamber. By using mylar diaphragms between the "target" chamber and the blast tanks as shown in Figure 1, the "target" chamber can be evacuated to the desired encounter pressure while the blast tanks are evacuated to a very low pressure.

The range provides for 335 cm of projectile free flight from gun muzzle to interception of the stream of water droplets at the photographic instrumentation port.

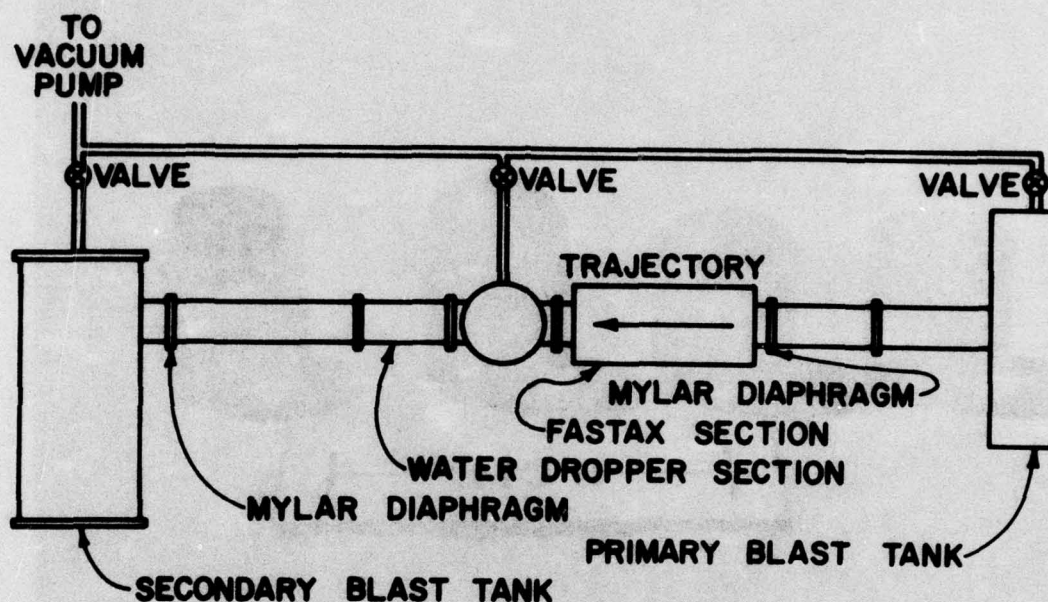


Figure 1. A schematic of the range used for erosion studies.

A Hall velocity measuring system placed 244 cm from the muzzle consists of two 0.25 mm slits, placed 61 cm apart perpendicular to trajectory, through which focused light is imaged on to the film plane of a streak camera.\* As the projectile passes each slit the light is temporarily blocked and an image of the projectile is recorded on the film. The film speed and projectile image separation are accurately measured and together with the slit separation are used to calculate projectile velocity.

The projectiles used in this study were 20 mm diameter one caliber long lexan cylinders with various shaped leading ends as shown in Figure 2. The light gas gun is capable of launching projectiles of 10 g to 5.5 km/s but for this study the velocity was maintained at 3.6 km/s to 4.9 km/s.

\*Wollensak 16 mm Fastax.



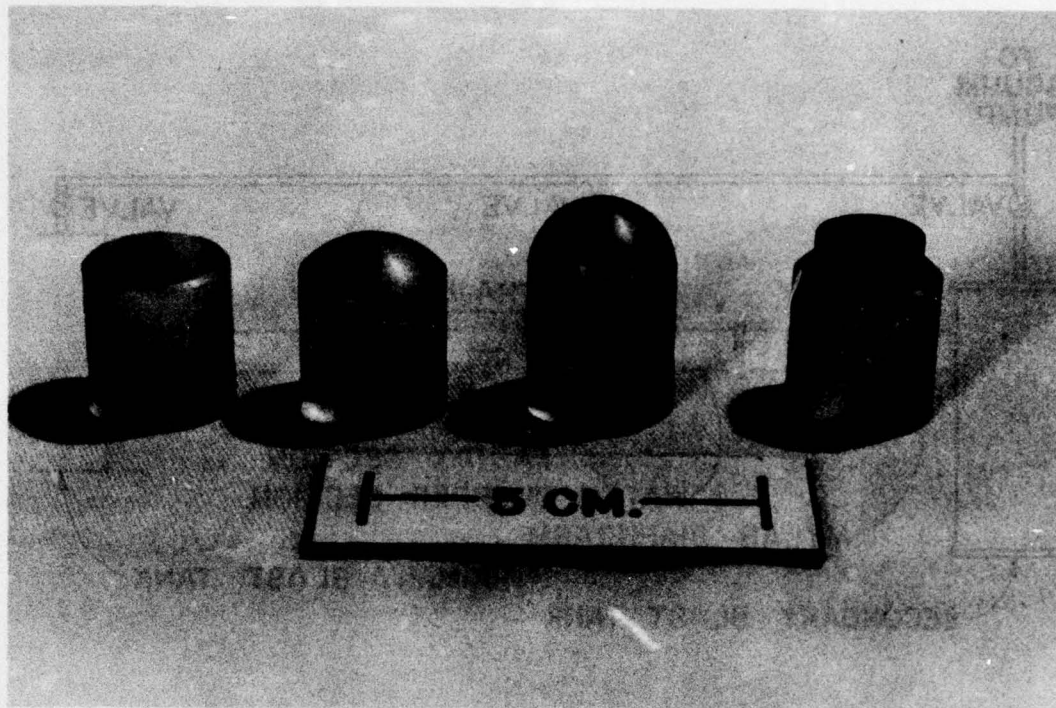


Figure 2. Typical projectiles used in the water drop/bow shock interaction investigation.

## 2.2 IMAGE CONVERTER CAMERA SYSTEMS

### 2.2.1 Single Camera System

An image converter camera\* was used in the initial phase of the test program. The camera is capable of obtaining very short exposure times (5-30 ns). A single image converter camera with a light source\*\* and condenser was used as a shadow graph system as shown in Figure 3. The field of view was 1 cm diameter and the overall object to film plane magnification was 9:1. The camera optical axis was on a horizontal

\*Beckman & Whitney Model No. 500

\*\*Beckman & Whitney Model No. 5401

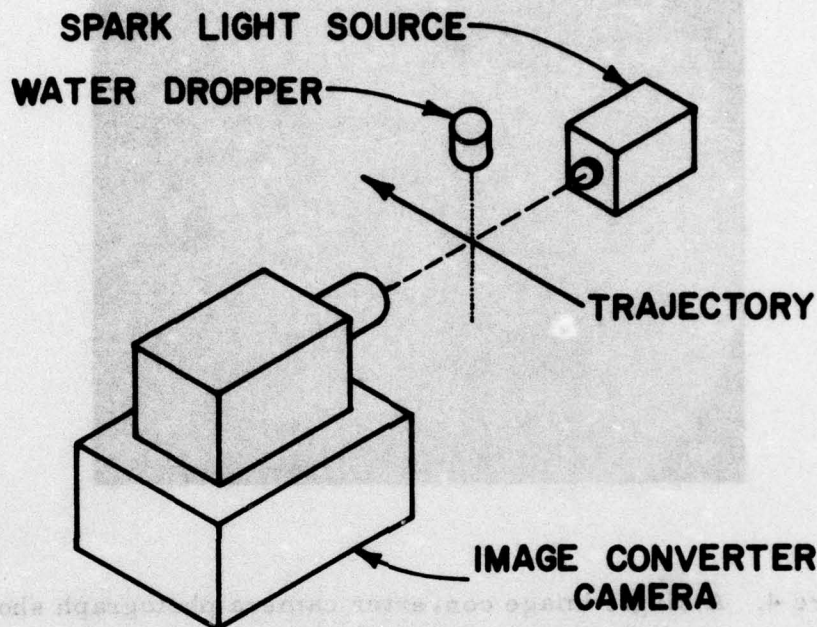


Figure 3. Single image converter camera shadow graph system.

plane with, and normal to, the projectile trajectory axis. A stream of 200  $\mu\text{m}$  diameter water drops was arranged to pass vertically down through the optical axis/ projectile trajectory intersection as illustrated in Figure 3.

A HeNe laser beam with a diameter of 1 mm was aligned to pass diagonally through the center of the field of view and onto the sensing element of a transient light detector. Interruption of the laser beam produced a signal from the light detector which was amplified to 1 KV and used to trigger the image converter camera and light source.

Typical photographs obtained with this system are displayed in Figures 4 and 5. The projectile nose, the bow shock, the water drops and impact debris plumes were observed.



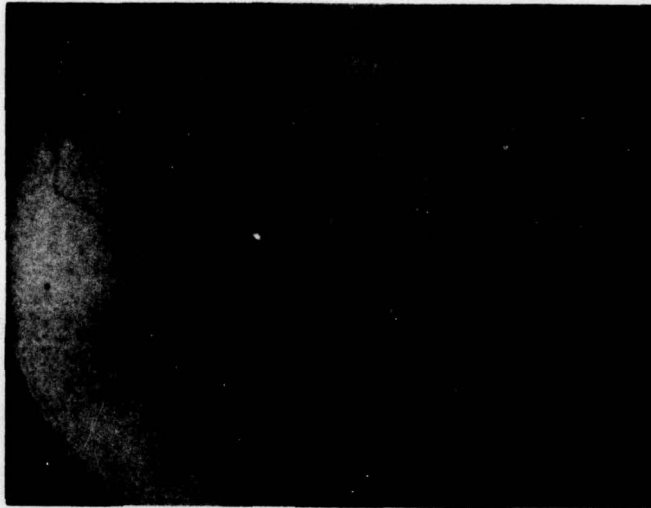


**Figure 4. A single image converter camera photograph showing small drops traversing the bow shock.**

3412  
3838 m/s  
1 cm. rad. nose  
mag. 8.3 : 1

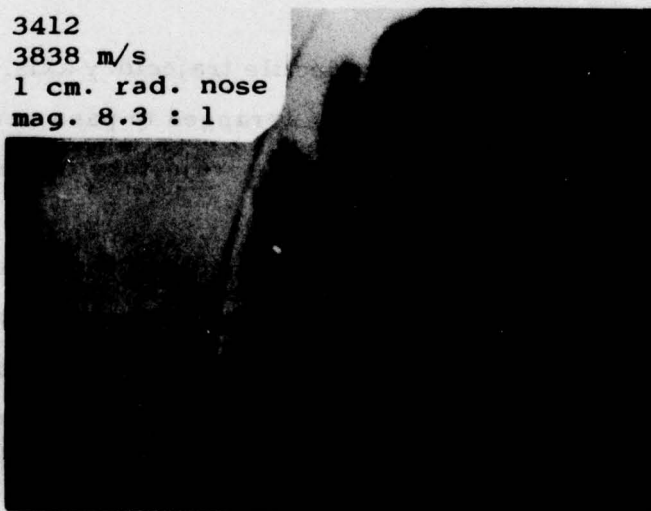


**Figure 5. A single image converter camera picture showing impact debris plumes.**

The single image converter system had the following capabilities and limitations:

- i) The image converter exposure time (5-30 ns) was sufficient to stop hypervelocity projectile motion.
- ii) Debris plumes generated by projectile/water drop impacts could be easily detected. (Figure 5)
- iii) Sequential photographs could not be obtained.
- iv) The image converter tube phosphor and the large grain high speed film produced low resolution photographs.
- v) Magnification was limited to 9:1 which was too low to detect minor changes of water drop shapes.

#### 2.2.2 Multiple Camera System

Four image converter cameras were arranged, as shown in Figure 6, so that each camera monitored the same field of view and the optics for each camera was the same for the single camera described in Section 2.2.1. The three pellicles were selected and positioned so as to evenly divide the light among the four cameras and a high energy 10  $\mu$ sec duration spark gap light source (16) provided illumination for the total photographic sequence. Peak light intensity was reached in 10  $\mu$ sec, followed by a slow decay. As the light economics of the four camera system required that the event be photographed at peak light intensity, the light source was triggered by the output of an up-down counter (discussed in Section 2.4) 10  $\mu$ sec before the event.

The camera triggers were initiated by the same method as for the single camera described in Section 2.2.1 and the interval between photographs was controlled by varying the delay time of each camera.

Sequential photographs were taken to determine the water drop size before the shock wave interception, water drop distortions during the shock wave/water drop interaction, and to observe debris

## IMAGE SPLITTING TECHNIQUE

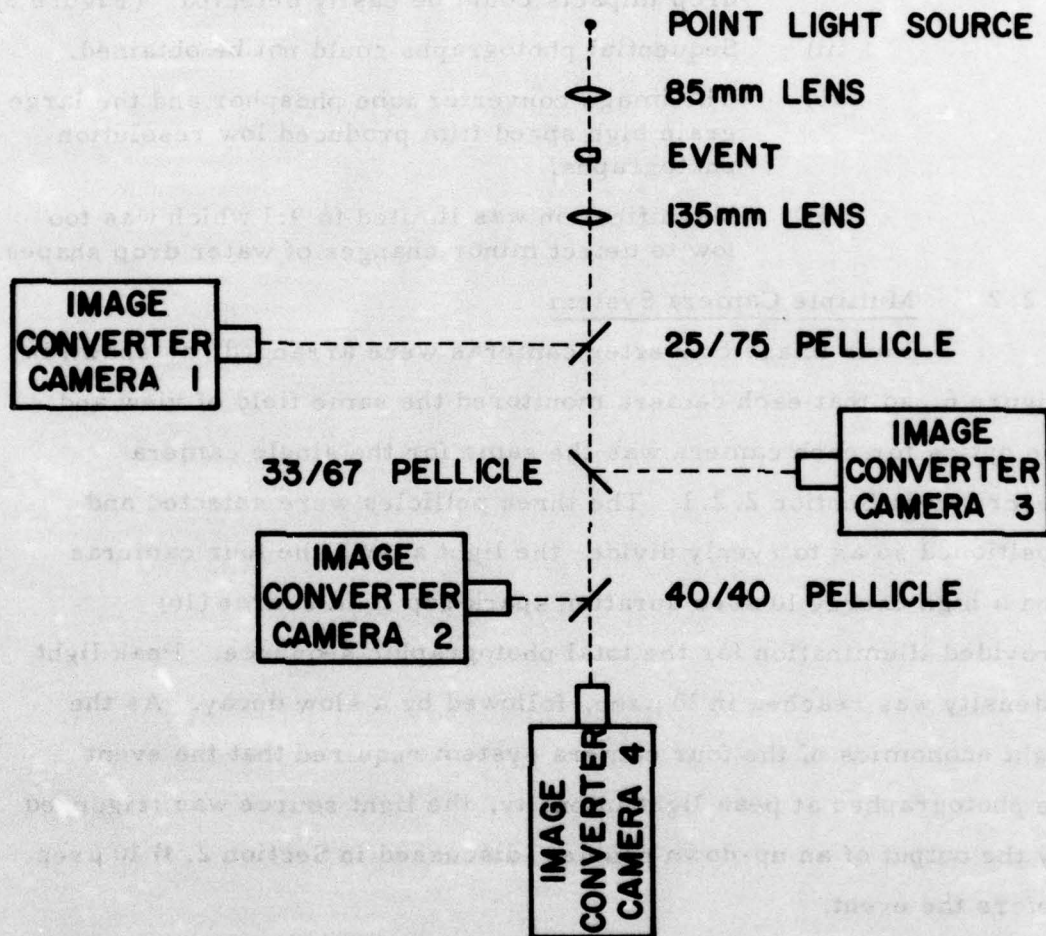
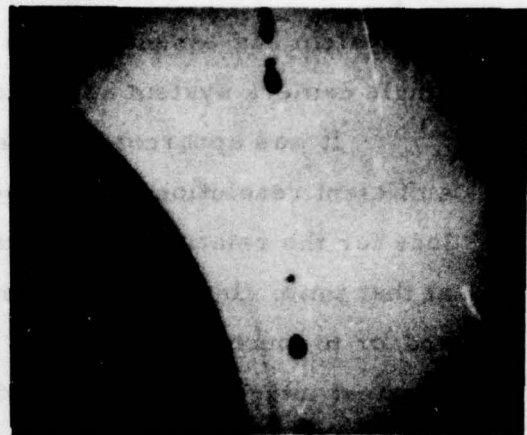
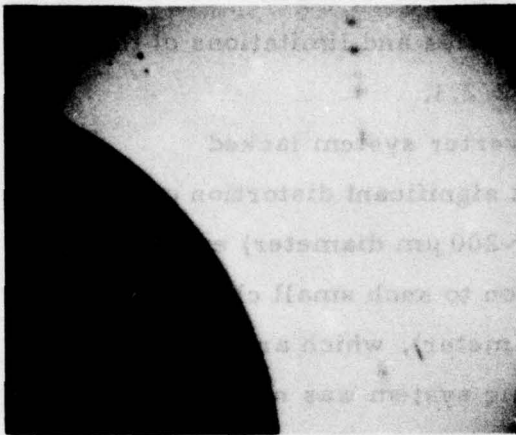


Figure 6. Four image converter camera system arrangement.

plumes after the projectile had impacted the drops. A typical sequence is displayed in Figure 7.

Shock waves associated with the water drops could not be detected nor minor deformation or mass stripping of the water





Shot no. 3485  
 Water drop diameter: 150  $\mu\text{m}$  Velocity 4.1 km/s  
 Projectile: 10 mm nose radius Range Pressure: 381 Torr  
 lexan

Figure 7. A typical four image converter camera system sequence.

drops measured. Although sequential photographs could now be obtained the system had essentially the same capabilities and limitations of the single camera system as listed in Section 2. 2. 1.

It was apparent that the image converter system lacked sufficient resolution to observe small, but significant distortion or mass loss for the relatively large water drops ( $\sim 200 \mu\text{m}$  diameter) employed at that time. In order to extend observation to such small changes and/or to much smaller drops ( $\sim 10 \mu\text{m}$  diameter), which are of the greatest interest, an improved photographic system was necessary.

### 2. 3 Q-SPOIL LASER/MICROSCOPE CAMERA PHOTOGRAPHIC SYSTEM

The inadequate resolution of the photographs obtained from the image converter camera systems prompted the search for a method of producing high resolution, high magnification photographs of projectile/water drop encounters.

#### 2. 3. 1 Microscope Camera

An optical system employing a 75 mm focal length lens and a 17 mm microscope eyepiece was assembled into the body of a 20.32 cm x 25.4 cm view camera to form an open shutter system capable of producing enlarged high resolution photographs. A schematic of the optics of the camera is shown in Figure 8. The system was typically operated at 18:1 magnifications. A narrow pass notch filter\* was placed between the object plane and the camera lens to eliminate extraneous light from the laser light source.

#### 2. 3. 2 Q-Spoil Laser

A Q-spoiled laser system\*\* was used as a light source for the microscope camera. The laser is a rail mounted modular type and its principal characteristics are as follows:

\*Atomic Optics

\*\*Holobeam Model No. 6082



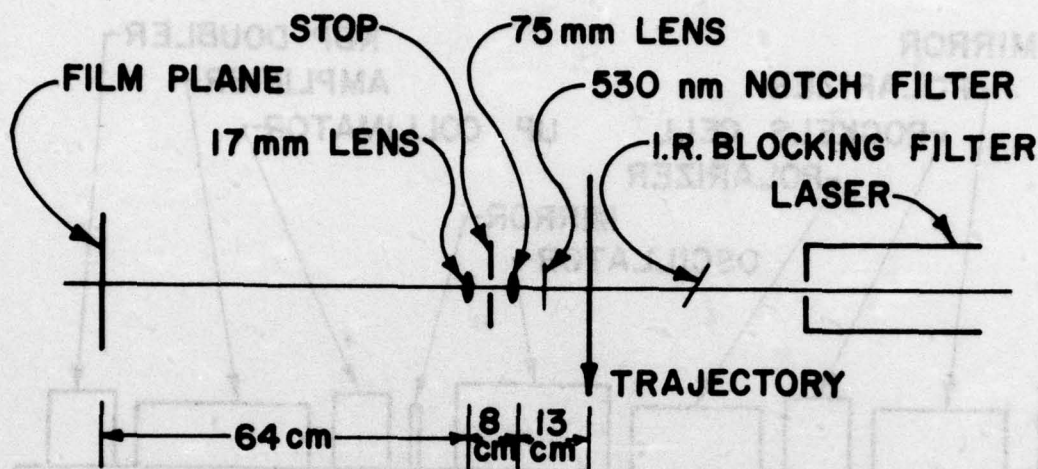


Figure 8. A schematic of the optics of the microscope/laser camera system.

- i) The lasing medium is Nd glass.
- ii) The output at 1060 nm is 14 J.
- iii) The output is frequency doubled into the visible (530 nm).
- iv) The output of KDP doubler at 530 nm is 1 J.
- v) The duration at half power points is 15-30 ns.
- vi) The beam diameter is 1.91 cm.
- vii) The optimum pump time is  $500 \pm 100 \mu\text{s}$ .

The KDP doubled output of 530 nm is used for back lighting the field of view in this set of experiments. A diagram of the Q-spoiled laser system is shown in Figure 9.

The axis of the microscope/Q-spoiled laser camera system is located perpendicular to the projectile and water drop axis as shown in Figure 10. A photograph of the complete assembly on the range is shown in Figure 11.

A photograph, obtained with this system, of water drops traversing a bow shock is displayed in Figure 12 and a selection of other photographs obtained is collected in Appendices B and C.

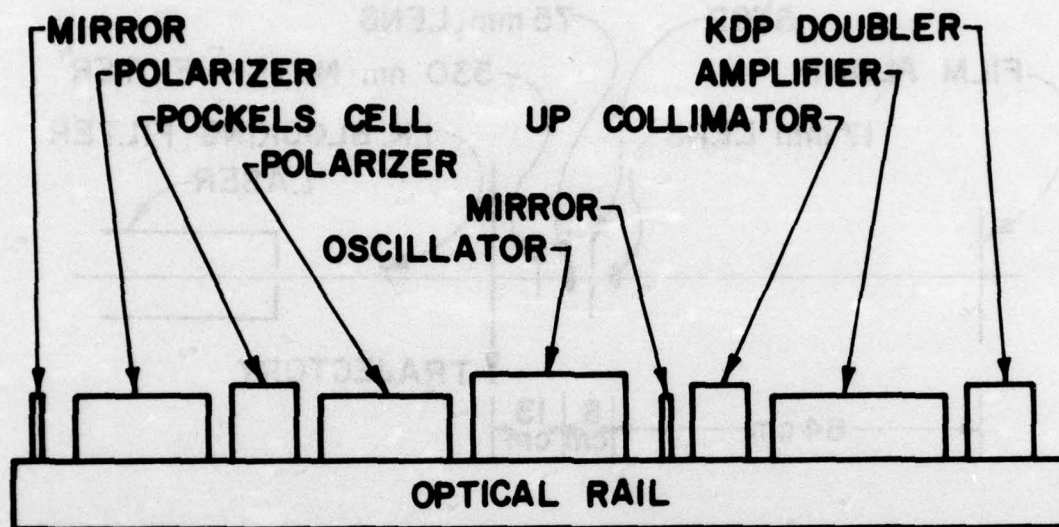


Figure 9. The Q-spoiled laser.

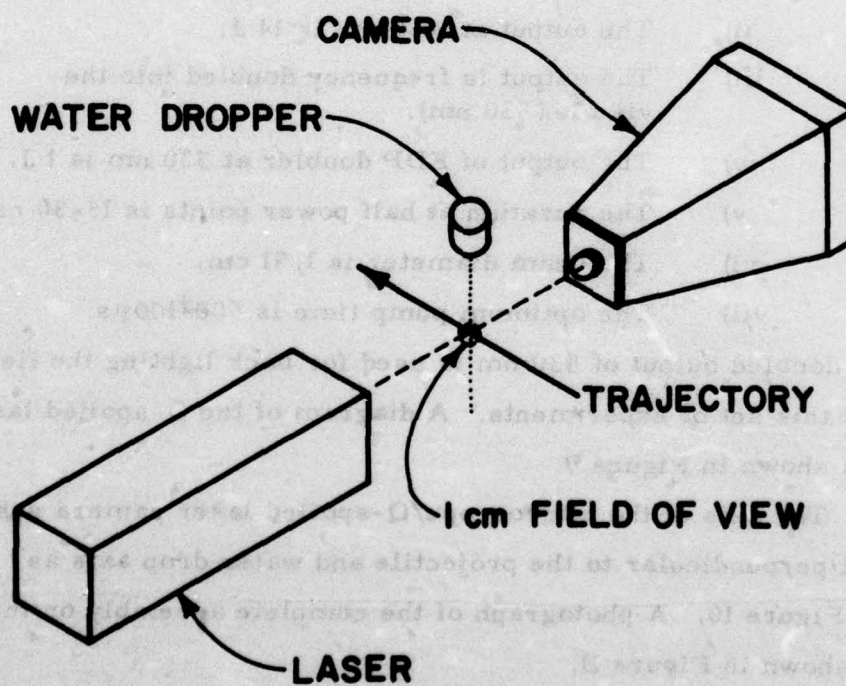


Figure 10. A schematic of the microscope/Q-spoiled laser camera system.

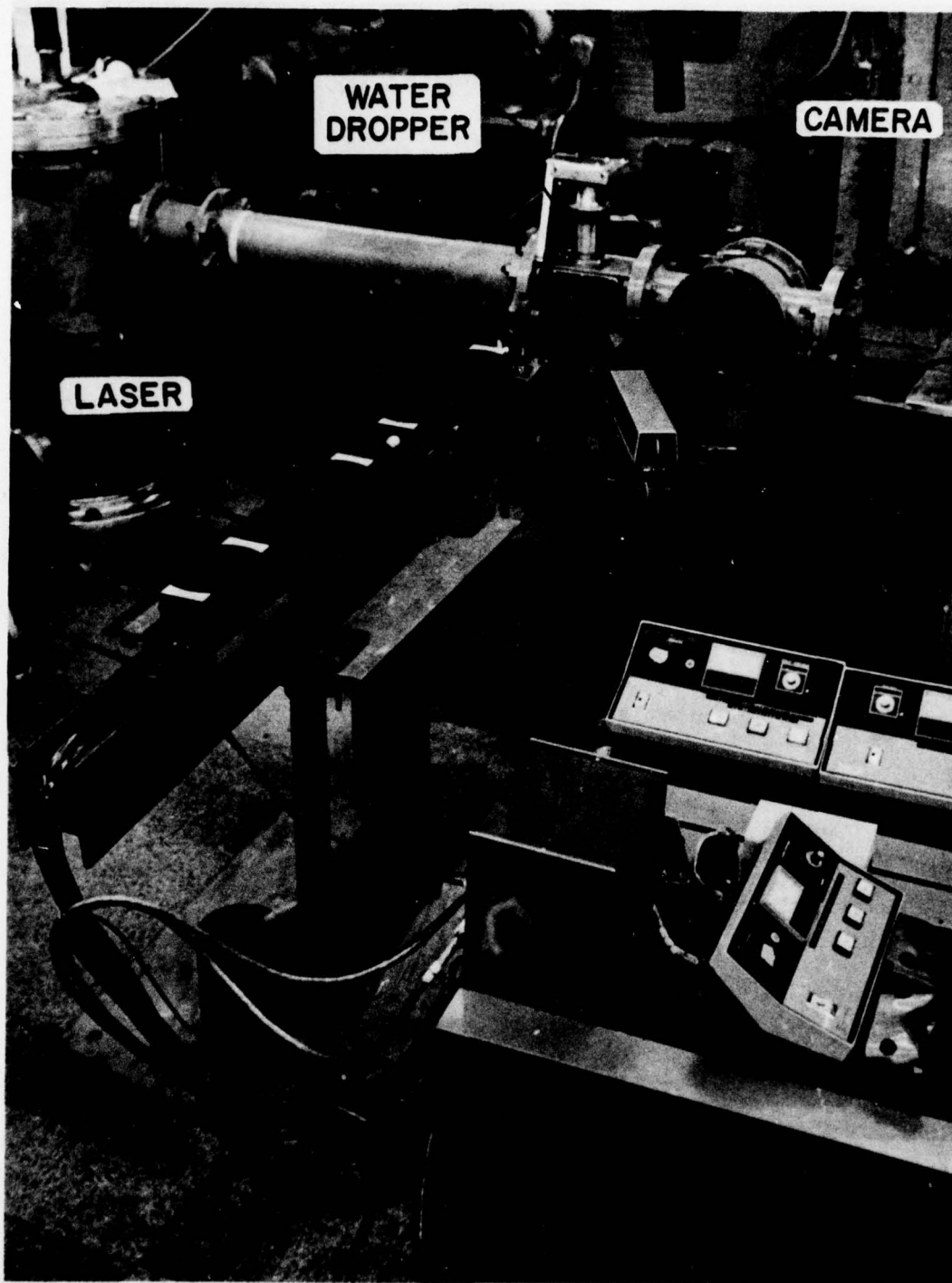
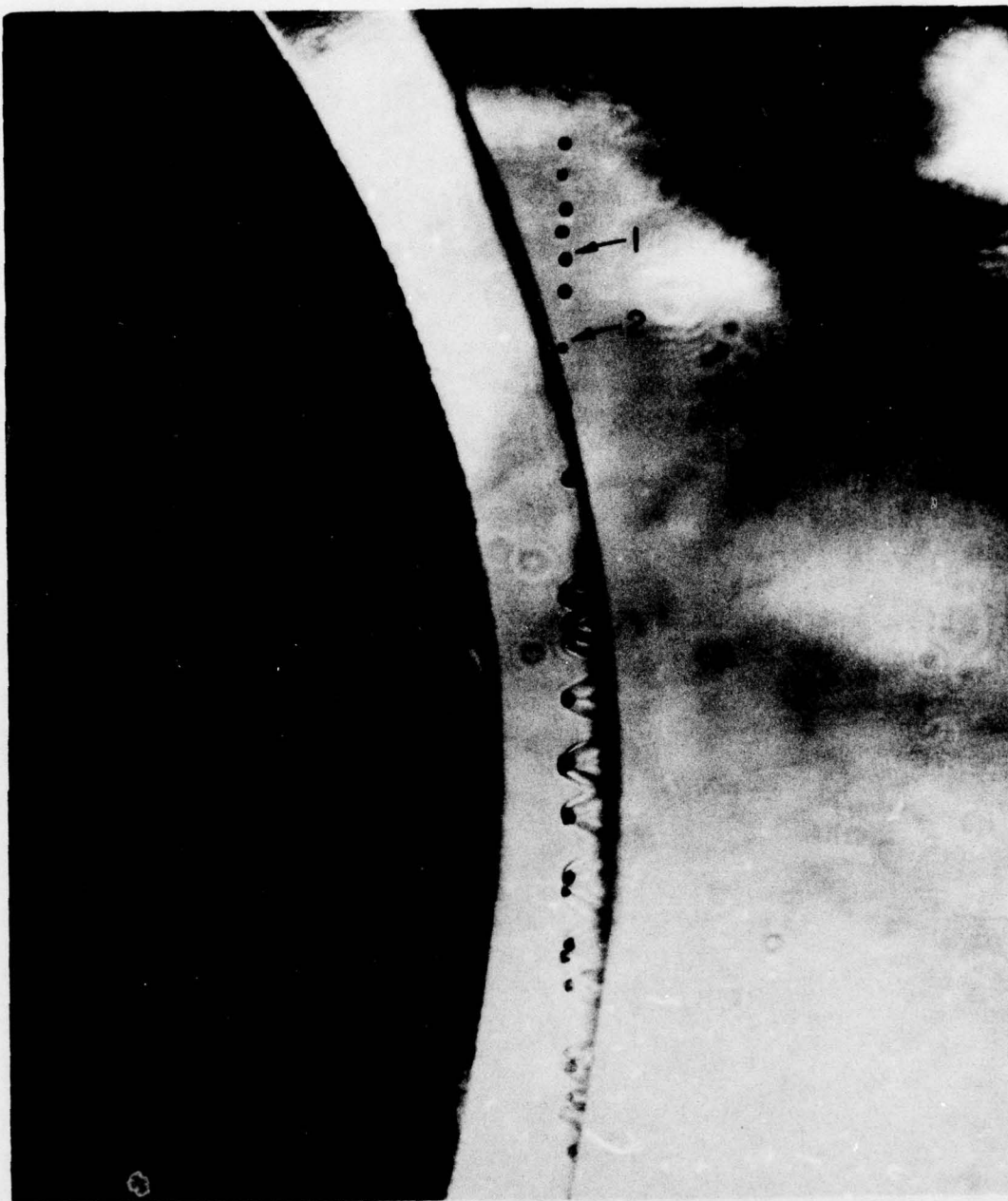


Figure 11. A photograph of the microscope/Q-spoiled laser camera system on the range.





Shot no. 3581

Water drop diameter:

1) 111  $\mu\text{m}$

2) 82  $\mu\text{m}$

Projectile: 12.7 mm nose  
radius lexan

Velocity: 4.0 km/s

Range Pressure: 508 Torr

Figure 12. A photograph of water drop/bow shock interaction obtained with the microscope/Q-spoiled laser camera.

Water drops down to  $\sim 5 \mu\text{m}$  diameter can be resolved with medium fine grain film.

#### 2.4 TRIGGERING TECHNIQUES

In order to observe the water drop/bow shock interaction it was necessary to pulse the laser after the drops have traversed the bow shock but before impact with the projectile nose tip. A typical elapsed time between the instant the shock wave reaches the stream of water droplets until the projectile impacts the drops was 250 ns for the conditions of interest (shock standoff of  $\sim 1 \text{ mm}$ , projectile velocity  $\sim 4 \text{ km/s}$ ).

Triggers are generated by projecting a HeNe laser beam across the projectile trajectory onto a transient light detector. Interruption of the laser beam by the oncoming projectile produces a trigger signal from the transient light detector. The transient light detectors used in this study have an overall time delay of 200 ns but have low jitter (20-50 ns).

In using the transient light detector to trigger the image converter cameras described in Section 2.2, the delay time was compensated by properly positioning the HeNe laser beam.

For the microscope Q-spoiled laser camera system, an up-down counter was used in conjunction with two HeNe laser beam/transient light detector stations to compute the precise time of arrival of the projectile at the water drop stream as illustrated in Figure 13. The up counter is started when the projectile breaks the first laser beam, and the up counter is turned off and down counter is started as the second laser beam is broken. The down count begins immediately thereafter with the accumulative total of the up counter and proceeds to subtract from the up counter total until zero is reached and a trigger signal is generated. The counting ratio of the up and down counters can be adjusted to match the inverse of the distance ratio of the trigger separation to the distance from down count trigger to the

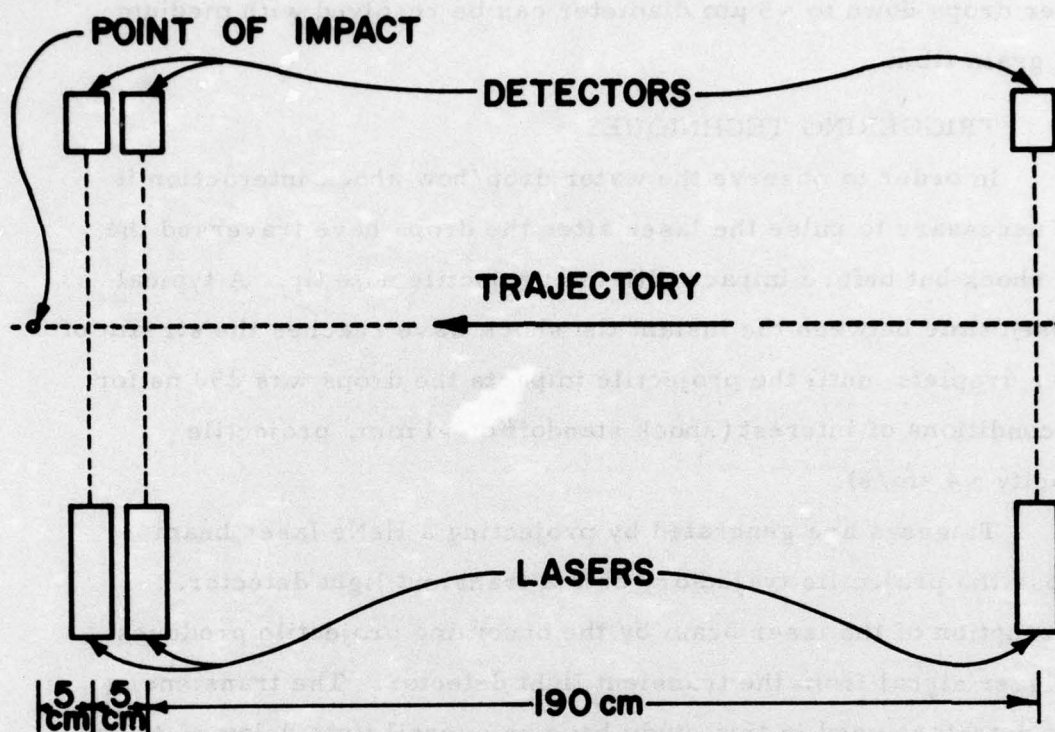


Figure 13. A schematic of the up-down counter trigger system.

event. The up-down counter clock oscillates at a frequency of 10 MHz and with the up to down count ratio equal to one the maximum jitter is  $\pm 10$  ns.

The up-down counter is used, with the trigger arrangement as shown in Figure 13, as a computer to provide accurate timing for the Q-spoiled laser pockel cell trigger. The Q-spoiled laser pump cycle is triggered by a HeNe laser/transient light detector  $500 \pm 50$   $\mu$ s before the laser cavity is spoiled.

## 2.5 WATER DROP GENERATOR

The water drop generator\* used throughout most of this study and illustrated in Figure 14 was a pressure driven, crystal vibrated,

\*Developed by Aerotherm Corporation



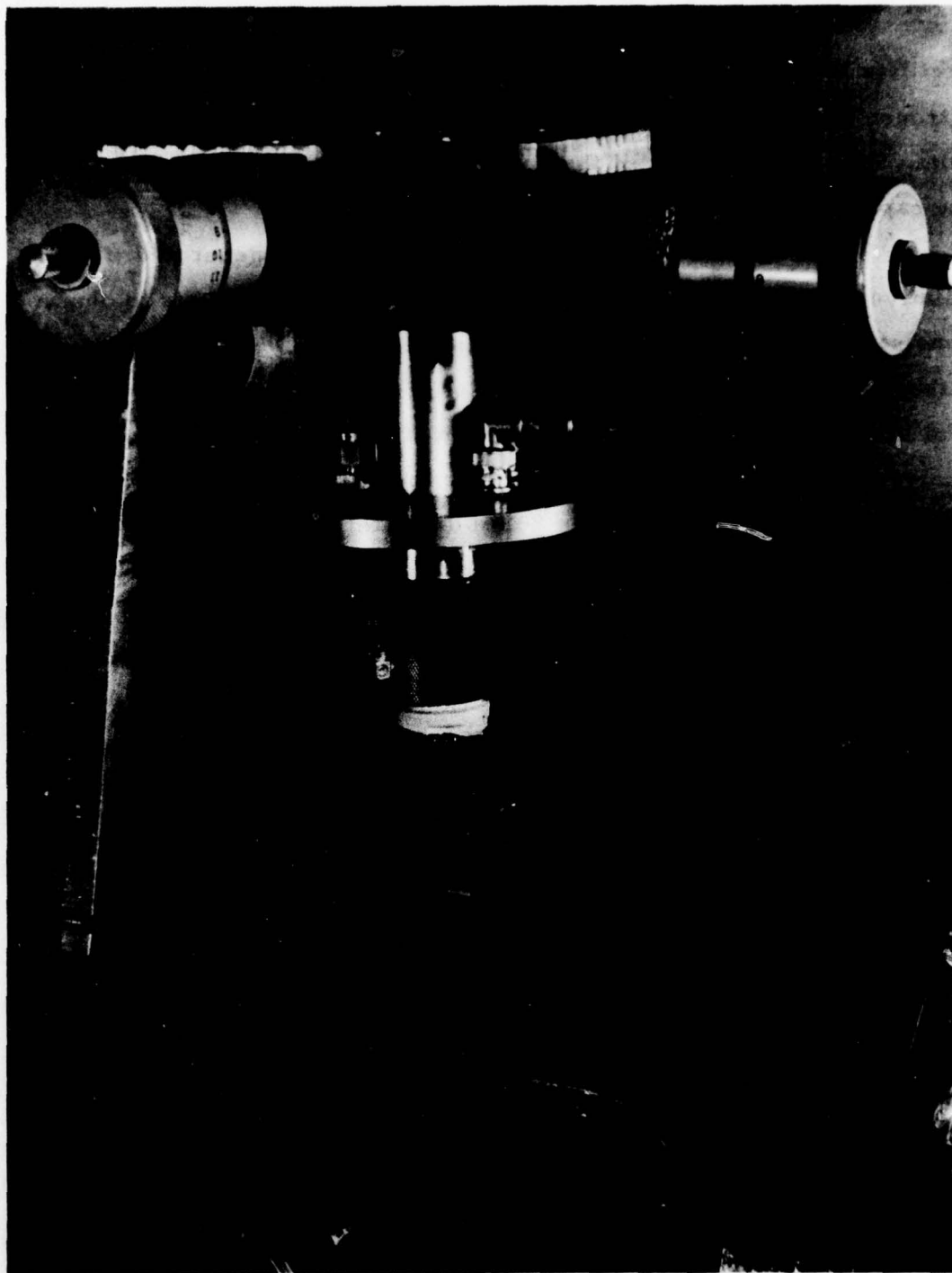


Figure 14. The vibrating capillary water drop generator.

microsyringe filter housing with a capillary tip\* output. An inverted prefilter housing\*\* filled with distilled water and pressurized with nitrogen gas, served as an accumulator/pressure chamber. Two inline 5 $\mu$ m filters provided the final filtration and served to prevent the capillary from clogging.

Water drops of 80-200  $\mu$ m diameter could be generated with relative ease but were not always uniform in size. Attempts to obtain consistent drop size less than 80 $\mu$ m diameter have been unsuccessful, although sprays of water drops down to  $\sim$ 15  $\mu$ m diameter were obtained. The erratic size and spatial distribution of these fine sprays made analyses of the data very difficult. The lower useful limit of drop size was therefore regarded as 80 $\mu$ m diameter.

After preparation of this report began a vibrating orifice drop generator\*\*\* was obtained which was capable of producing single streams of much smaller drops (down to  $\sim$ 10  $\mu$ m diameter). A second camera was also added to the range to obtain a photograph of the drops immediately prior to impact. It will now be possible to obtain reliable data on much smaller drops.

\*Tempress Research Co. Part #5110-10S

\*\*Millipore Corporation #YY13

\*\*\*Thermosystems Corporation. Model 3050

## SECTION 3

### ANALYTIC INVESTIGATION

#### 3.1 INTRODUCTION/OBJECTIVE

An analytical effort was initiated to examine the physics of the processes observed in the experimental portion of the research program. In conducting this effort, emphasis was placed upon both isolating the predominant physical mechanisms responsible for droplet destruction and performing calculations which would assist in directing the experiments. The latter objective determined the limits of the physical conditions which were considered. These limits are summarized in Table 1.

Table 1. RANGE OF PHYSICAL CONDITIONS STUDIED

Droplet Size	20 to 200 $\mu$ m diameter
Equivalent Altitude	3.05 to 6.1 km
Vehicle Velocities	Mach 5 to Mach 20
Vehicle Nose Radius	1.0 cm

Prior to initiating any analysis, a review was undertaken of previous experimental and theoretical studies which might relate to the current problem. While a completely thorough review was impossible due to time and budget constraints, an effort was made to become familiar with the work of those investigators who made significant past contributions or who were currently working on the problem of droplet fragmentation. In addition, representative literature relating to particle drag, heat transfer, and vaporization in high temperature high velocity flow were considered.

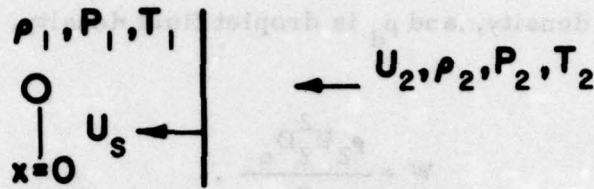


We concluded from this review, that it was unlikely that any purely theoretical analysis would predict the fragmentation phenomena with sufficient accuracy to be of value to the current effort. The reason for this viewpoint was twofold: first, the simplifying assumptions employed in previous theoretical analysis raised serious questions as to validity and, secondly, any new theoretical analysis would be too complex to conduct during the allotted time, and would not provide the desired assistance to the experimental program. For this reason, we decided to rely on previously developed empirical correlations of droplet fragmentation for the current analysis. A brief summary of these correlations is presented in Section 3.2.

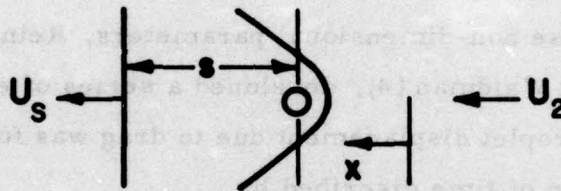
### 3.2 EXPERIMENTAL STUDIES

The physical problem which is to be described, simplified to one dimensional flow, is illustrated in Figure 15. A droplet of diameter,  $D_0$ , is initially stationary with respect to the surrounding atmosphere. A shock wave is approaching the droplet from the right with a velocity,  $U_g$ . The gas behind the shock wave is moving with a lower velocity  $U_2$ . The time clock is started ( $t=0$ ) when the shock wave just reaches the droplet. At some time,  $t$ , later the shock wave has moved past the droplet a distance  $S=U_g t$ . During this time the droplet has been displaced a distance,  $x$ , due to shear and pressure forces and has acquired a velocity  $U_d$ . In addition, the droplet deforms so that its frontal diameter,  $D$ , is greater than its initial diameter  $D_0$ , and its mass,  $m$ , is less than its initial mass  $m_0$ . If the Mach number of the shock is sufficiently large, the flow past the droplet is supersonic and a bow wave persists until the droplet has been accelerated so as to make the relative flow subsonic.

This problem has been studied experimentally using one dimensional shock tubes (1-7), and empirical correlations were developed to describe the droplet fragmentation process. There are two principal fragmentation modes of interest to the present problem, stripping and catastrophic breakup. The stripping mode appears to be



15(a)



15(b)

Figure 15. A schematic of water droplet/bow shock interaction.

controlled by the shear forces acting on the droplet so that mass is continually eroded or "stripped" away. The catastrophic mode occurs suddenly and is characterized by large unstable surface waves which help tear the droplet apart. Both the stripping and catastrophic modes of break-up can be correlated by using an appropriate set of nondimensional parameters. These are:

droplet displacement  $X$ ;

$$X = x/D_0, \quad (1)$$

time  $T$ ;

$$T = \frac{U_2}{D_0} \left( \frac{\rho_2}{\rho_d} \right)^{1/2} t, \quad (2)$$



where  $\rho_2$  is gas density, and  $\rho_d$  is droplet fluid density, and Weber number  $W$ ;

$$W = \frac{\rho_2 U_2^2 D_o}{\sigma_d}, \quad (3)$$

where  $\sigma_d$  is the droplet surface tension prior to passage of the shock wave. Physically, the Weber number,  $W$ , is the ratio of the dynamic pressure forces acting on the droplet to the surface tension forces holding the drop together. The larger the Weber number the more important the catastrophic breakup mode becomes.

Using these non-dimensional parameters, Reinecke and McKay (3), and Reinecke and Waldman (4), developed a series of experimental correlations. Droplet displacement due to drag was found to be a nearly quadratic function of time described by,

$$X = 0.8T^2, \quad (4)$$

which implies that the droplet acceleration is constant. Studies by Ranger and Nichols (5) indicate that even though this correlation represents a good fit to the data, there is a weak dependence upon Mach number.

The mass-time history of droplets during the stripping mode has been measured by x-ray absorption techniques (4). These data can be approximated with a cosine function of the form,

$$\frac{m}{m_o} = \frac{1}{2} \left\{ 1 + \cos \left( \frac{\pi T}{T_s} \right) \right\}. \quad (5)$$

The time,  $T_s$ , in the equation corresponds to the completion of stripping ( $m/m_o = 0$ ) and is found by Waldman and Reinecke to be,

$$T_s = 3.5. \quad (6)$$

(A slightly larger value ( $T_s = 5$ ) was obtained by Ranger and Nicholls who employed a less direct measure of droplet disintegration. The value measured by Waldman and Reinecke was used in this study.)

Catastrophic break-up of a droplet is described as occurring suddenly at a time,  $T_c$ , which is dependent upon Weber number (4),

$$T_c = 45W^{-1/4}. \quad (7)$$

Only when  $T_c$  is less than  $T_s$  will the catastrophic mode play a part in the fragmentation process. The condition for catastrophic break-up may be written as;

$$T_c = 45W^{-1/4} < 3.5 \quad (8)$$

or

$$\frac{\rho_2 U_2^2 D_o}{\sigma_d} > 2.73 \times 10^4. \quad (9)$$

Catastrophic break-up is therefore promoted by both increasing gas velocity and droplet diameter. The actual occurrence of catastrophic break-up also requires that  $T_c$  be smaller than the time to droplet impact.

### 3.3 PHYSICAL PROCESS

Although the fragmentation process may be described by the empirical correlations presented above, an evaluation of the physical conditions surrounding a droplet as it is overcome by a shock layer was conducted. Prior to entering the shock layer the droplet is assumed to be at rest relative to the surrounding atmosphere. The only manner the droplet can sense the coming events is via the radiant heat flux reaching it from the shock layer and calculations indicate that the heating which occurs during this period is negligible, even at high Mach numbers ( $M=15$ ).

A qualitative picture of a typical droplet inside a shock layer is presented in Figure 16. For the range of physical conditions of interest the Mach number of the droplet relative to the shock layer gases will depend principally upon the location of the droplet within the shock layer and only weakly upon the vehicle velocity and free stream



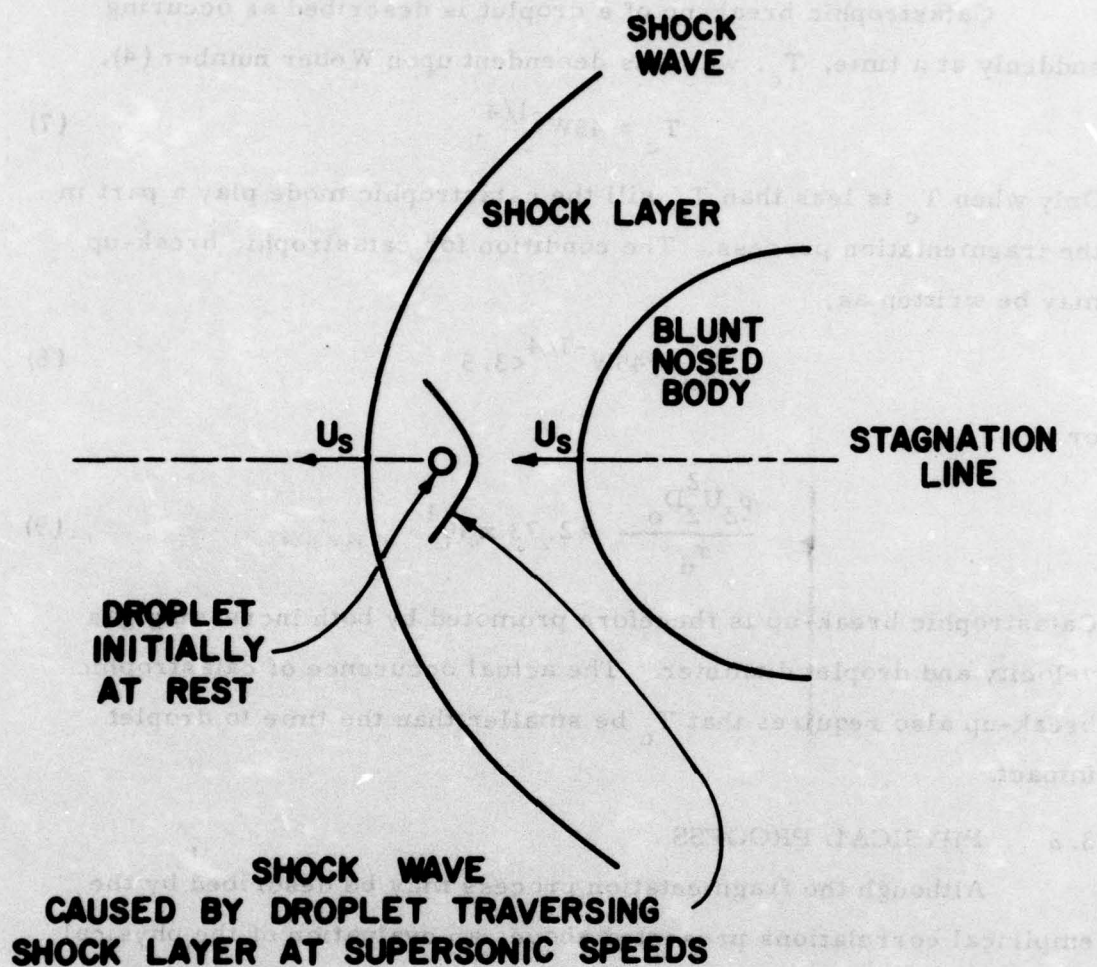


Figure 16. A schematic of a water droplet in the shock front.

pressure. The droplet Mach number just after entering the stagnation region of the shock layer is shown in Figure 17 as a function of free stream pressure and vehicle Mach number. The data used for these calculations assume an ambient temperature of  $300^{\circ}\text{K}$  and account for imperfect gas effects (9). The gas immediately surrounding the droplet is double shocked and is at a higher temperature, pressure and density than the gas in the vehicle shock layer.

For an ambient pressure equal to that at an altitude of 6 km and vehicle Mach numbers greater than about 7, the stagnation

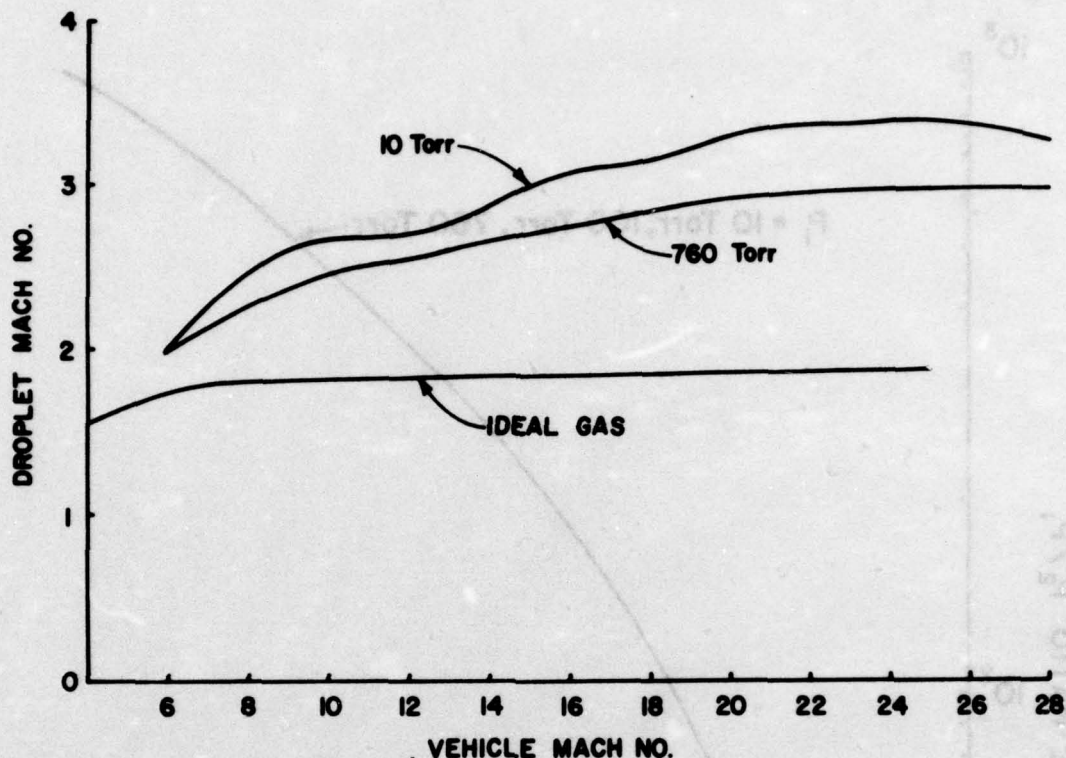


Figure 17. Droplet Mach number as a function of vehicle Mach number.

point pressure on the droplet surface will exceed the critical pressure for water.

The gas conditions existing in the stagnation regions of the vehicle shock layer just inside the shock wave are illustrated in Figures 18, 19 and 20. These data were obtained from reference (9) and account for real gas effects.

### 3.4 SHOCK STANDOFF DISTANCE

To verify the optical system calibration and check the theoretical calculations, it was decided to compare shock standoff distance,  $\Delta$ , in front of the projectile against theoretical predictions. The experimental data obtained from enlargements of photographs of projectile produced shocks were reduced in the form of  $\Delta/R_N$  where  $R_N$  is the nose radius. These data are presented in Figure 21. The theoretical



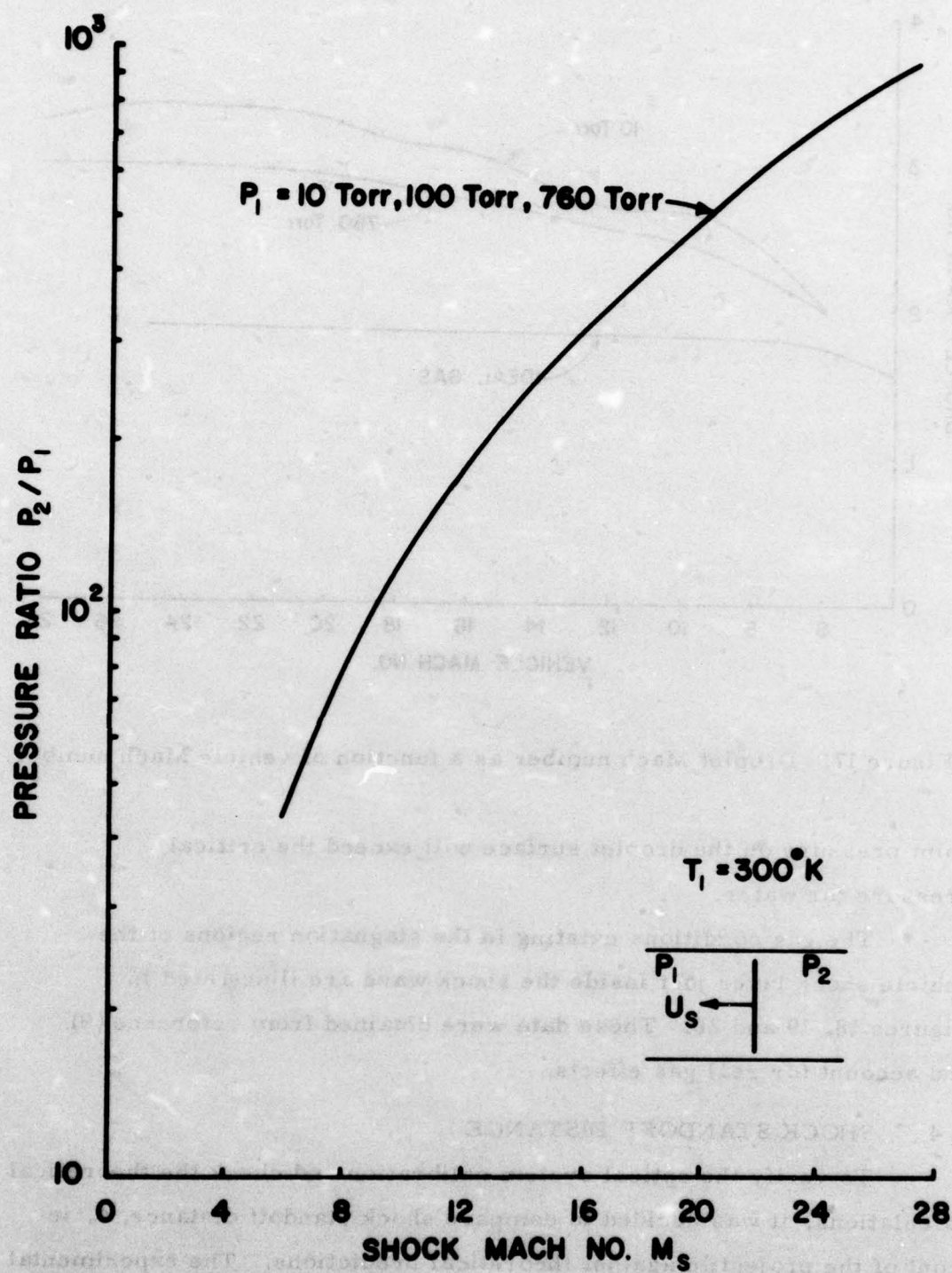


Figure 18. Pressure ratio across the shock.

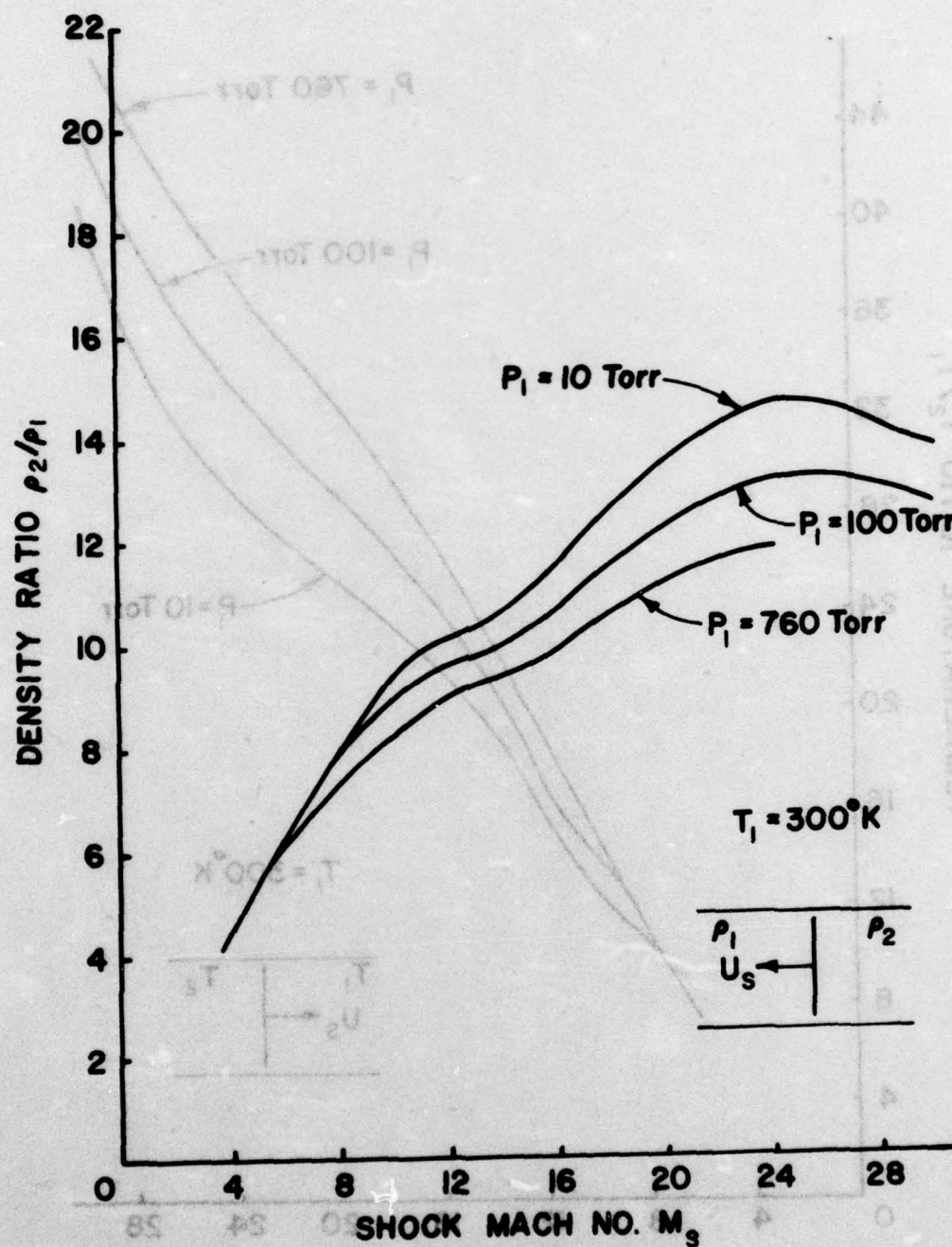


Figure 19. Density ratio across the shock.



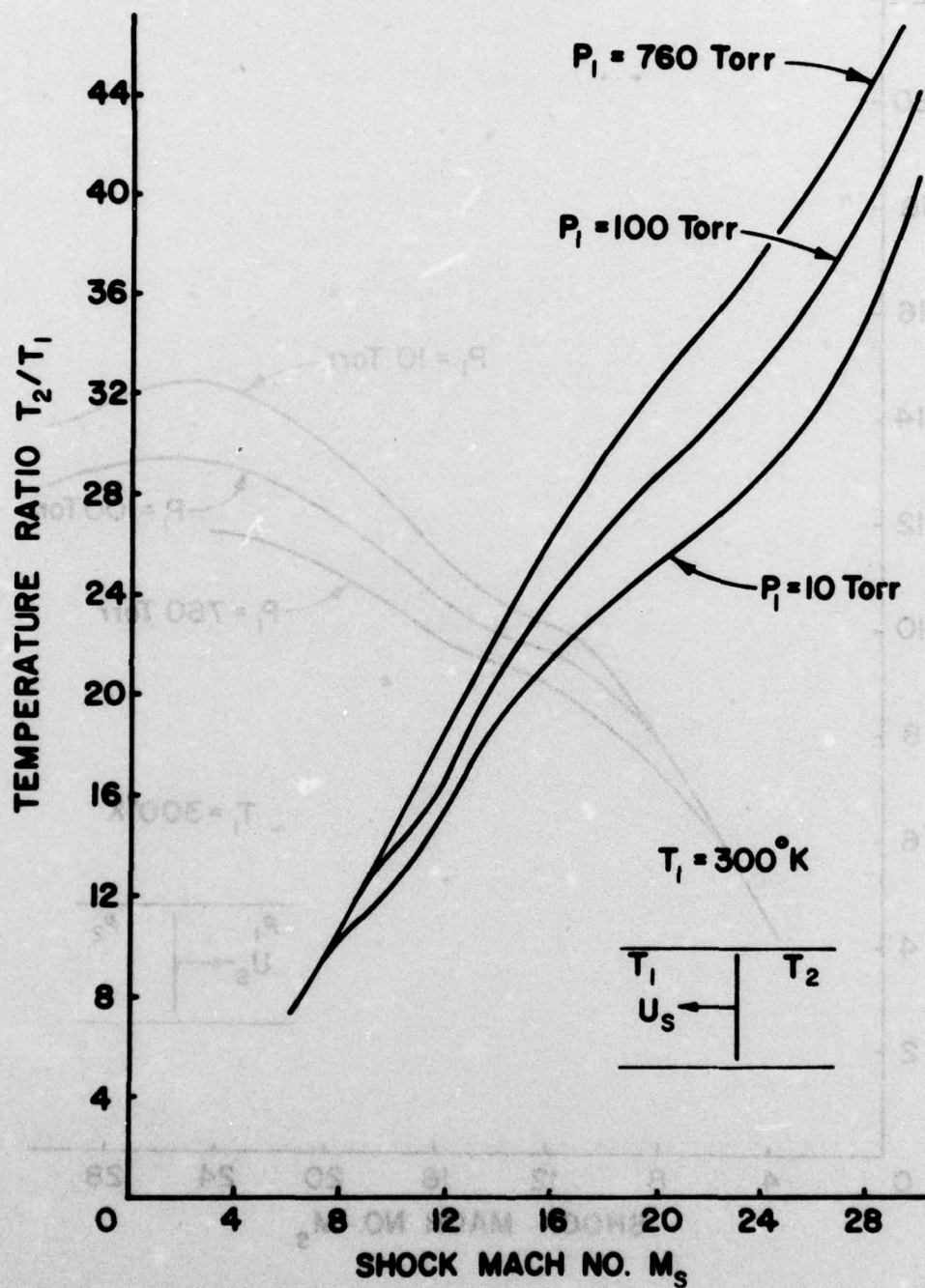


Figure 20. Temperature ratio across the shock.

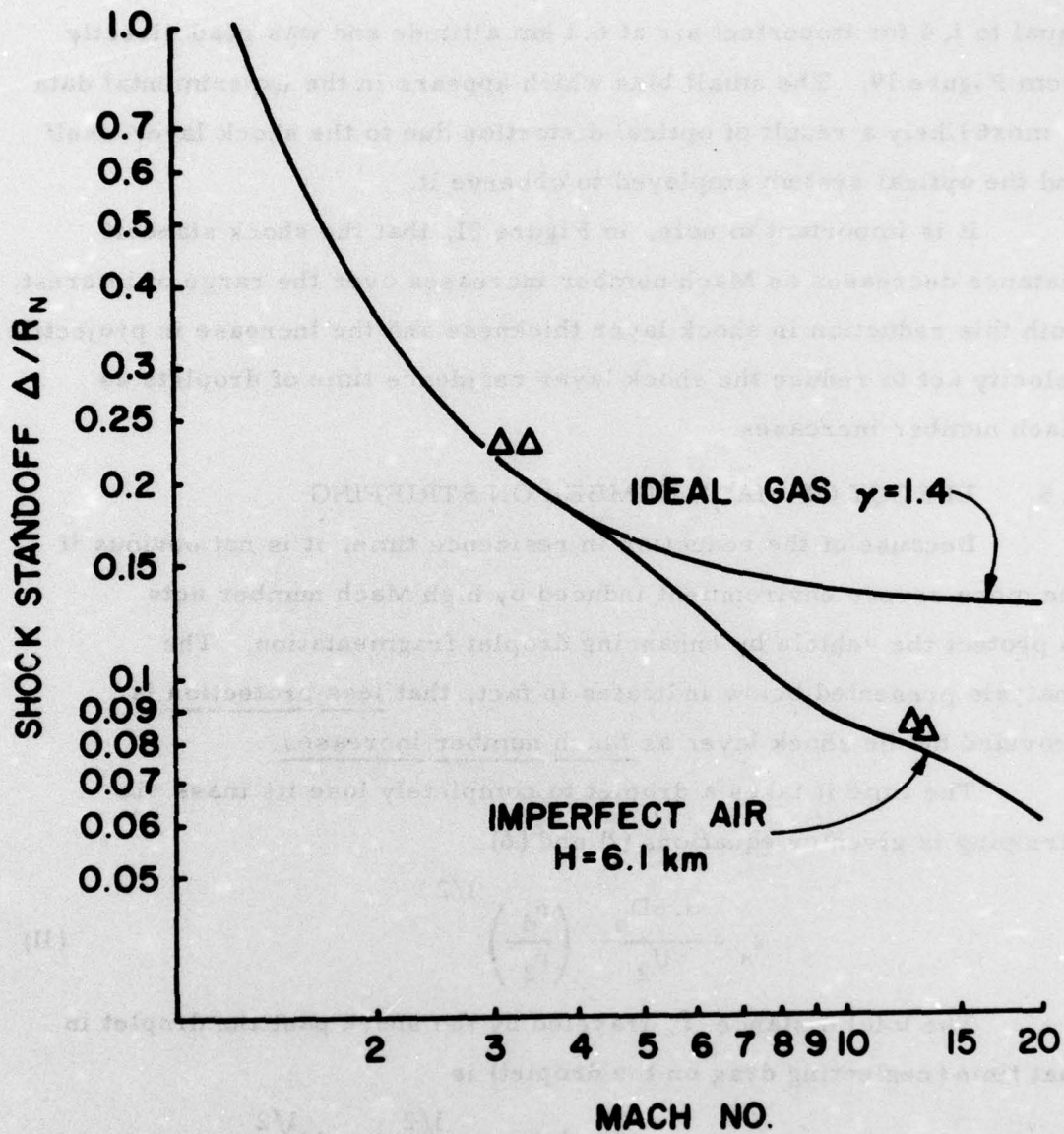


Figure 21. Shock standoff distance as a function of projectile Mach number.

curves were obtained by using the relation;

$$\frac{\Delta}{R_N} = 0.78\varepsilon \quad (10)$$

where  $\varepsilon = \rho_1/\rho_2$  is the density ratio across the shock wave. The density ratio was calculated for an ideal gas with  $\gamma$ , the ratio of specific heats,



equal to 1.4 for imperfect air at 6.1 km altitude and was read directly from Figure 19. The small bias which appears in the experimental data is most likely a result of optical distortion due to the shock layer itself and the optical system employed to observe it.

It is important to note, in Figure 21, that the shock standoff distance decreases as Mach number increases over the range of interest. Both this reduction in shock layer thickness and the increase in projectile velocity act to reduce the shock layer residence time of droplets as Mach number increases.

### 3.5 EFFECT OF MACH NUMBER ON STRIPPING

Because of the reduction in residence time, it is not obvious if the more severe environment induced by high Mach number acts to protect the vehicle by enhancing droplet fragmentation. The analysis presented below indicates in fact, that less protection is provided by the shock layer as Mach number increases.

The time it takes a droplet to completely lose its mass via stripping is given by equations (2) and (6).

$$t_s = \frac{3.5D_o}{U_2} \left( \frac{\rho_d}{\rho_2} \right)^{1/2} \quad (11)$$

The total distance,  $l$ , traveled by the shock past the droplet in that time (neglecting drag on the droplet) is

$$l = U_s t_s = 3.5D_o \left( \frac{U_s}{U_2} \right) \left( \frac{\rho_1}{\rho_2} \right)^{1/2} \left( \frac{\rho_d}{\rho_1} \right)^{1/2} \quad (12)$$

where  $U_s$  is shock wave velocity,  $\rho_1$  is free stream density and  $\rho_1/\rho_2 = \epsilon$  is the density ratio. The distance,  $l$ , may be compared to the shock wave standoff distance,  $\Delta$ , by employing equation (8).

$$l/\Delta = \frac{3.5D_o}{0.78R_N \epsilon} \left( \frac{U_s}{U_2} \right) \left( \epsilon \right)^{1/2} \left( \frac{\rho_d}{\rho_1} \right)^{1/2} \quad (13)$$

For a normal shock  $U_2$  is related to  $U_s$  by:

$$U_s/U_2 = 1/(1-\epsilon) \quad (14)$$

so that:

$$l/\Delta = 4.49 \left( \frac{D_o}{R_N} \right) \left( \frac{1}{\epsilon} \right)^{1/2} \left( \frac{1}{1-\epsilon} \right) \left( \frac{\rho_d}{\rho_1} \right)^{1/2} \quad (15)$$

The dependence of  $l/\Delta$  on Mach number in the preceeding equation is only through the density ratio which may be obtained from Figure 19 for imperfect air ( $\epsilon = \frac{\rho_1}{\rho_2}$ ). It is found that a twenty percent increase in  $l/\Delta$  occurs as Mach number increases from 6 to 14. Since the distance,  $l$ , to end of stripping increases relative to the shock layer thickness,  $\Delta$ , with Mach number we may infer that the mass fraction at impact also increases with Mach number.

This analysis neglects the possibility of catastrophic breakup, drag on the droplet, and changes in both gas density and velocity between the shock layer and the body. A more careful analysis which accounts for drag and catastrophic breakup was performed in the following manner.

The distance,  $S$ , between the droplet and shock wave at any time is given by:

$$S = U_s t - x \quad (16)$$

where  $x$  is the distance the droplet has been displaced due to drag. At impact  $S$  must equal the shock standoff distance

$$\Delta = U_s t_{\text{impact}} - x \quad (17)$$

By employing equation (4) for the drag distance, we can develop an expression for the time at which impact occurs. This may be used to compute mass lost to stripping and determine if catastrophic breakup has occurred. In addition, the impact velocity (or kinetic energy) may be computed from

$$V_{\text{impact}} = U_s - U_d \quad (18)$$

where  $U_d$  is computed by taking the time derivative for the expression, equation (5) for drag displacement.

$$U_d = \frac{dx}{dt} = 1.6 D_o \frac{T_{\text{impact}}^2}{t_{\text{impact}}} \quad (19)$$



Figures 22 and 23 present the mass fraction ( $m/m_0$ ) and kinetic energy fraction ( $KE/KE_0$ ) at impact for varying droplet diameter at both Mach 5 and Mach 20. Consistent with previous analysis, a greater fraction of the mass and kinetic energy reach the surface at higher Mach numbers. Thus, higher Mach numbers result in less erosion of the droplets prior to impact even when drag is accounted for.

The above analysis may be reversed to compute the initial droplet diameter which has zero mass at impact, or the droplet that has one-half its original mass at impact. This is accomplished by specifying the time at which the impact occurs. The results of these calculations are shown in Figure 24.

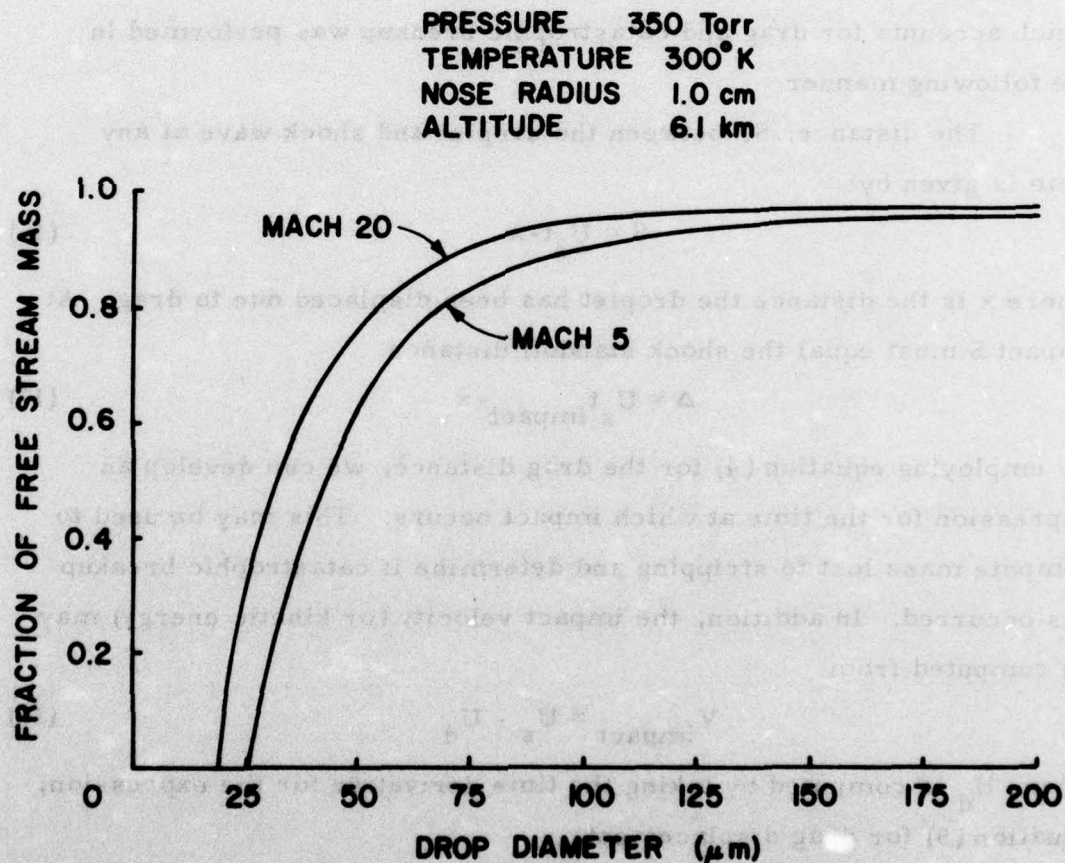


Figure 22. The mass fraction of droplet remaining at impact.

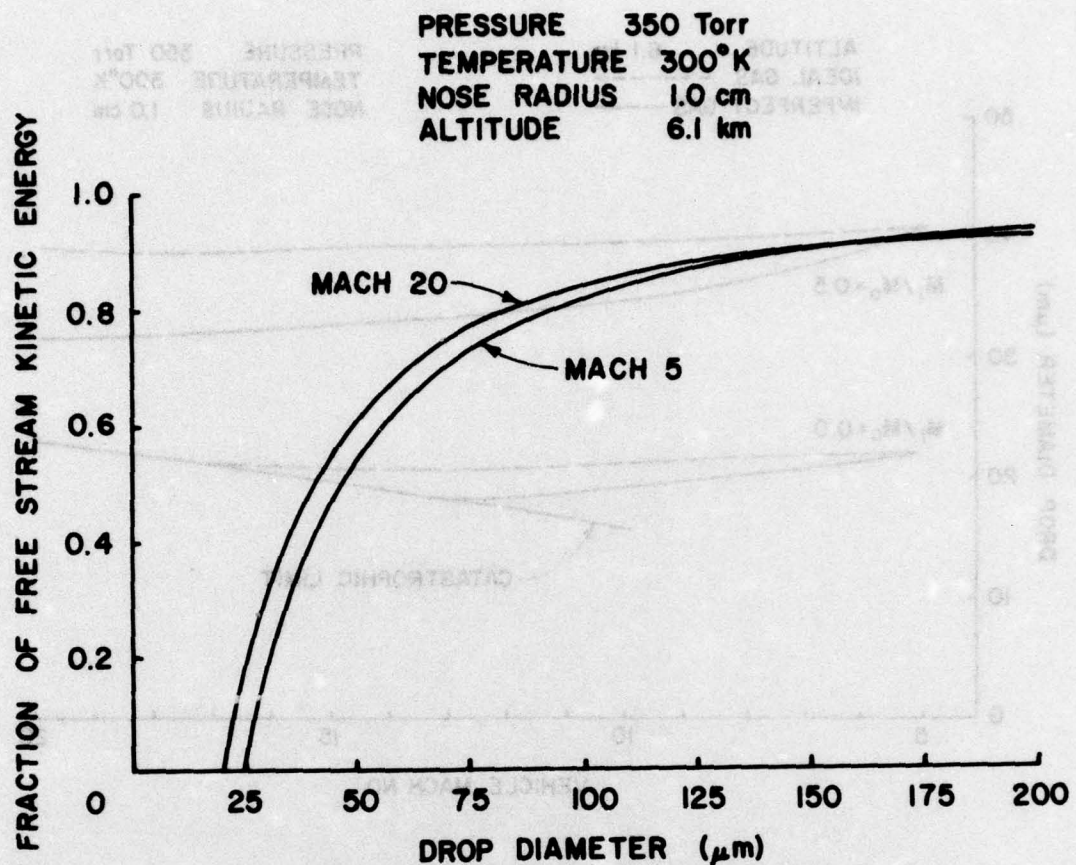


Figure 23. The droplet kinetic energy fraction remaining at impact.

The catastrophic limit shown in this figure indicates when a droplet will catastrophically break up just as it impacts. The correlations which have been previously presented indicate that catastrophic breakup occurs earlier in time as droplet diameter increases. While this is true for the nondimensional catastrophic breakup time,  $T_c$ , it is not true for real breakup time,  $t_c$ , which increases as droplet diameter is increased. This fact accounts for the shape of the catastrophic limit in Figure 24. As droplet diameter increases, catastrophic breakup is delayed. This is offset by increasing Mach number which reduces the time to breakup relative to the shock layer residence time.



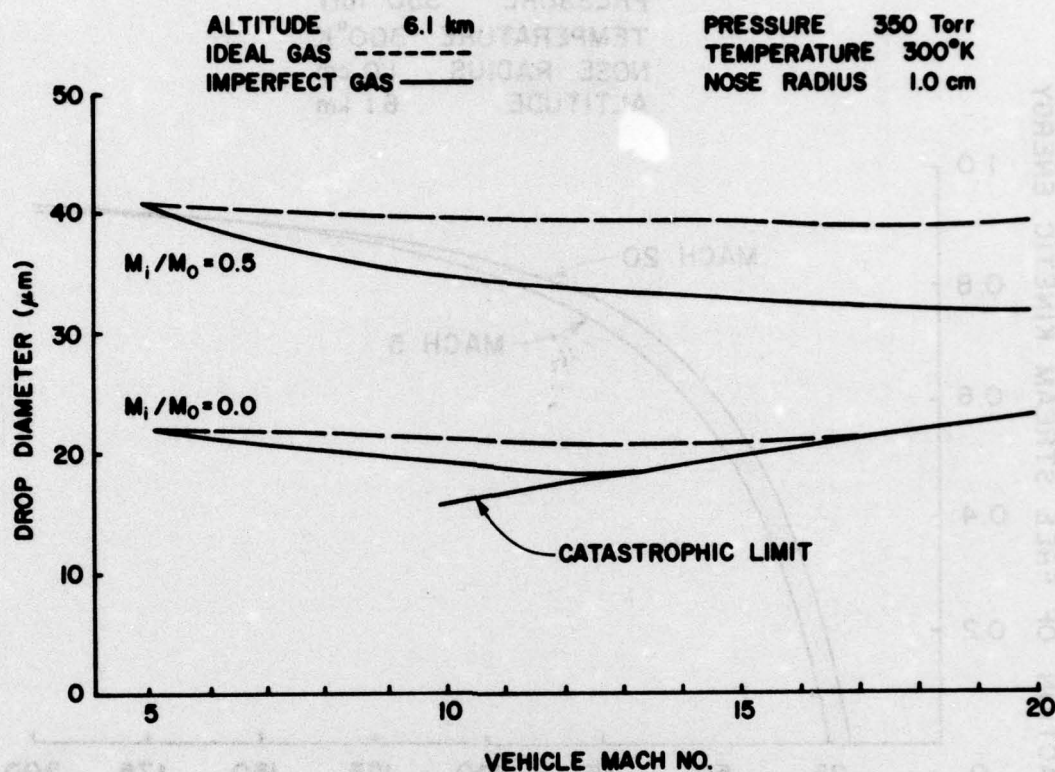


Figure 24. Droplet mass ratio remaining at impact as a function of initial drop size and vehicle Mach number.

### 3.6 TRAJECTORY STUDIES

Based on the previous analysis, it was decided to calculate the mass loss and trajectories of water droplets in the nose region. The question to which an answer was sought was, "What size droplet will be swept around the nose without impacting?"

The method employed to make the calculations was straightforward, but required knowledge of the gas density and velocity (magnitude and direction) throughout the flow field. This information was obtained by using a computer code developed by Northrop Corporation for the Air Force Flight Dynamics Laboratory (AFFDL), WPAFB (11), (12). The code calculates the inviscid flow field around supersonic/hypersonic spherically capped bodies. Real gas effects

are accounted for by using an effective ratio of specific heats in the calculations. The computer codes were obtained from Mr. J. Burke at AFFDL and were previously made operational on the CDC 6600 Computer System located at WPAFB. A recent change in system software, however, made the program non-operational, and it was necessary, to modify the program.

The equations which govern the time history of the droplet remain unchanged from those previously described. In order to compute the appropriate non-dimensional time for conditions of varying gas density and velocity, the approach proposed by Debora (7), (8) was adopted. The relation between real time,  $t$ , and non-dimensional time,  $T$ , equation (2), is written in integral form:

$$T = \int_0^t \frac{U_2}{D_o} \left( \frac{\rho_2}{\rho_d} \right)^{1/2} d\tau \quad (20)$$

This integration is performed along the droplet trajectory, allowing  $U_2$  and  $\rho_2$  to vary. The trajectory in turn is determined by employing equation (3), to compute droplet acceleration due to drag.

$$a = 1.6 \frac{U_{rel}^2 \rho_2}{D_o \rho_d} \quad (21)$$

The direction of the drag is assumed to be along the direction of the relative velocity,  $U_{rel}$ , between the droplet and the shock layer gases.

$$U_{rel} = U_2 - U_d \quad (22)$$

The position,  $S$ , of the droplet at any time is obtained by employing the fourth order Runge-Kutta numerical integration algorithm to solve the equation of motion.

$$\frac{d^2 S}{dt^2} = a \quad (23)$$

In this procedure, the reference frame is shifted to body fixed coordinates so that the free stream gases and the droplet have an initial velocity of  $U_s$ .



The results of the trajectory analysis are indicated in Figure 25.

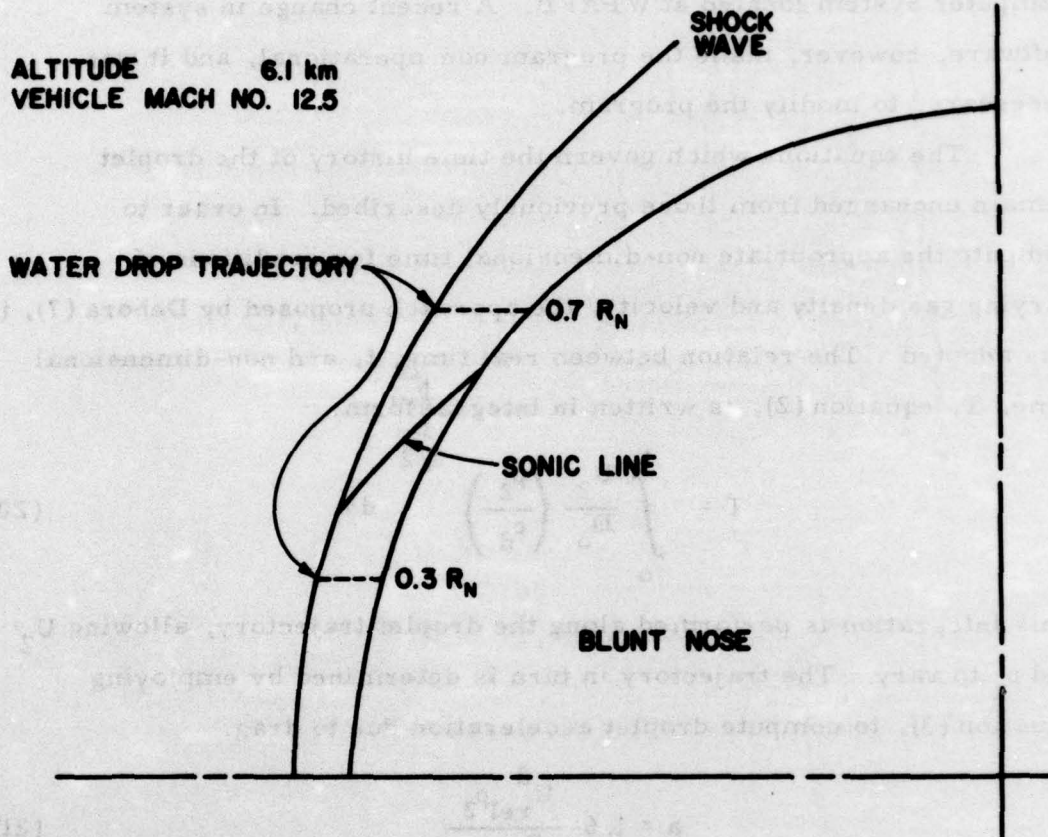


Figure 25. Trajectories of water drops at off axis positions.  
 $R = 0.3R_N$  and  $R = 0.7R_N$

Droplets of 10, 25, and 50  $\mu\text{m}$  diameter were entered into the shock layer at radial positions of  $R = 0.0$ ,  $R = 0.3R_N$  and  $R = 0.7R_N$ . In all cases the trajectories were not significantly deviated from a straight path. Typical mass and kinetic energy time-histories of the droplets are shown in Figures 26 and 27. It is seen that both the 50  $\mu\text{m}$  and 25  $\mu\text{m}$  droplets fully penetrate the shock layer while the 10  $\mu\text{m}$  droplet is completely fragmented about halfway through. The effects of drag

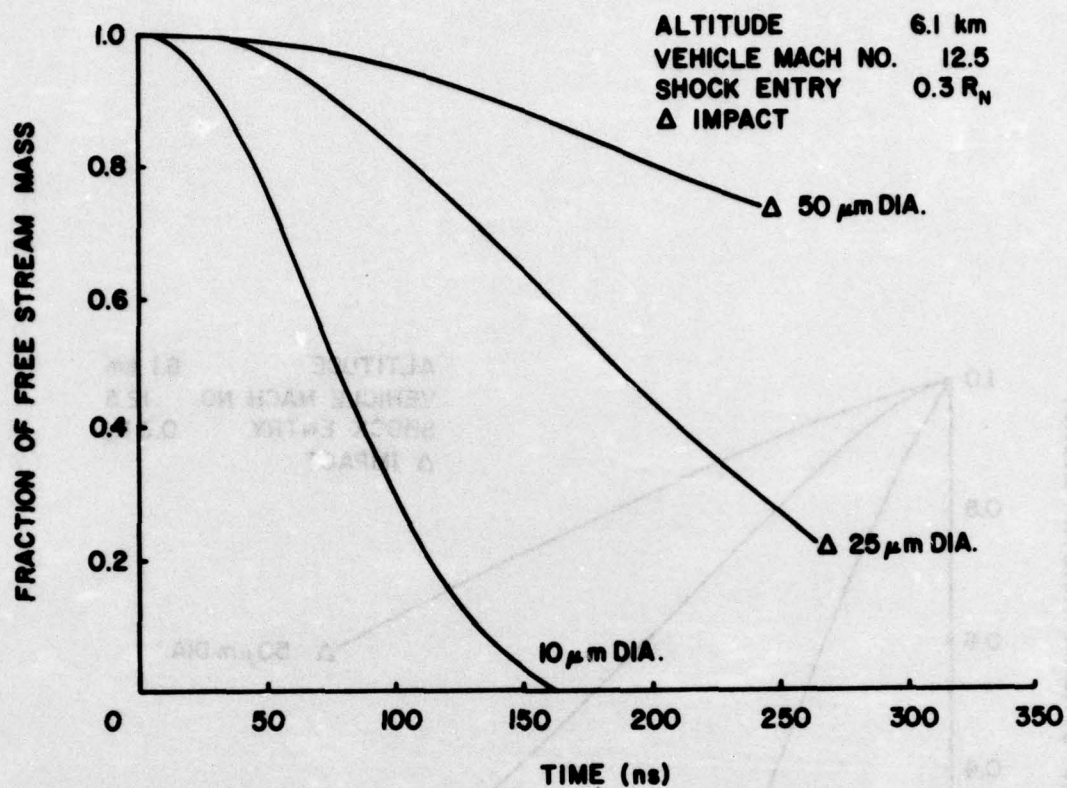


Figure 26. Mass fraction for droplets entering the shock off axis at  $R = 0.3 R_N$ .

on the droplet can also be seen in that the 25  $\mu\text{m}$  droplet takes a somewhat longer time than the 50  $\mu\text{m}$  droplet to penetrate the shock layer.



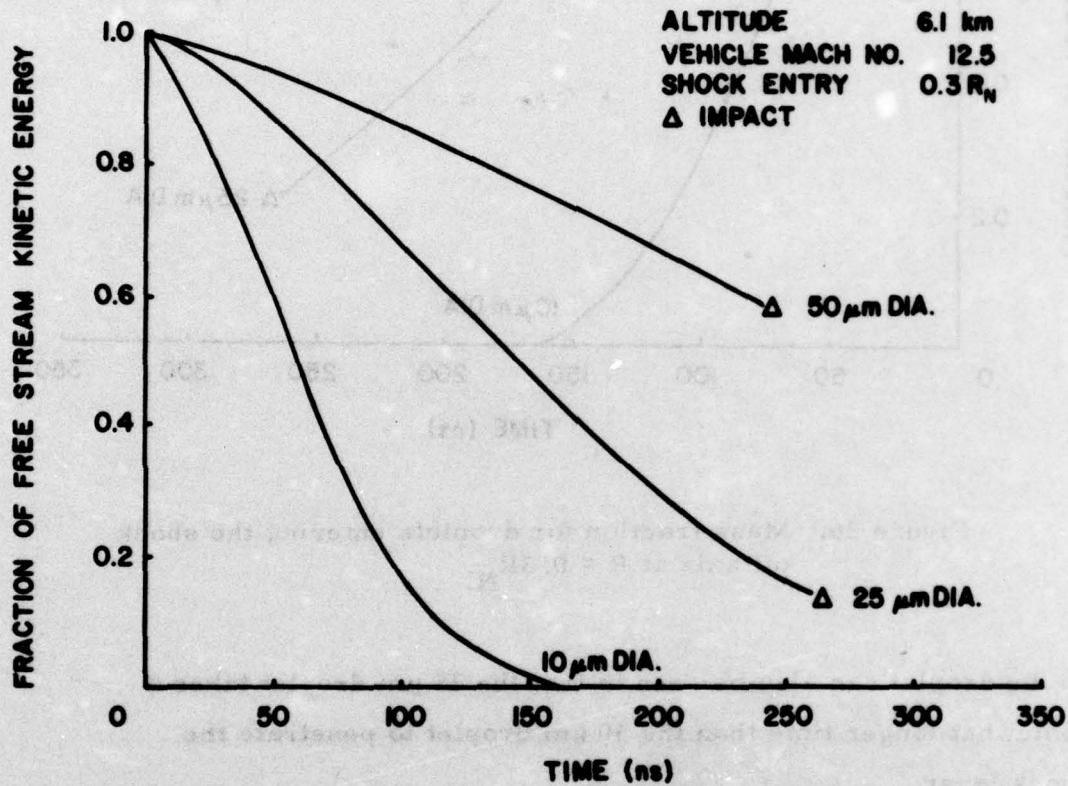


Figure 27. Kinetic energy fraction for droplet entering the shock off axis at  $R = 0.3 R_N$ .

## SECTION 4

### EXPERIMENTAL RESULTS

The experimental results are contained in or derived from photographs obtained of the water drop-shock wave interaction region. The investigation was directed to answering two questions:

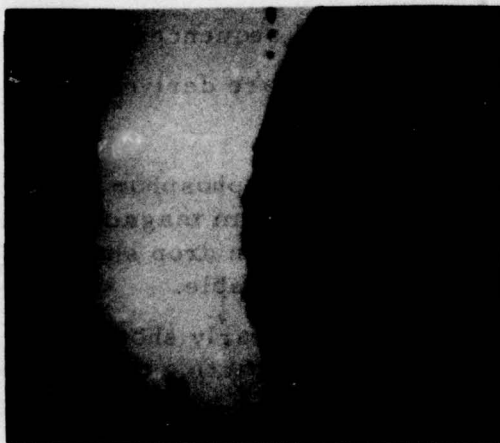
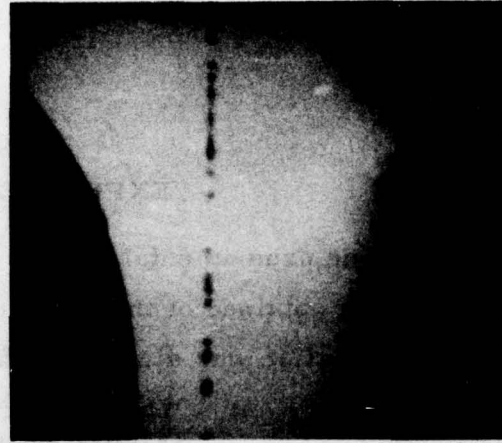
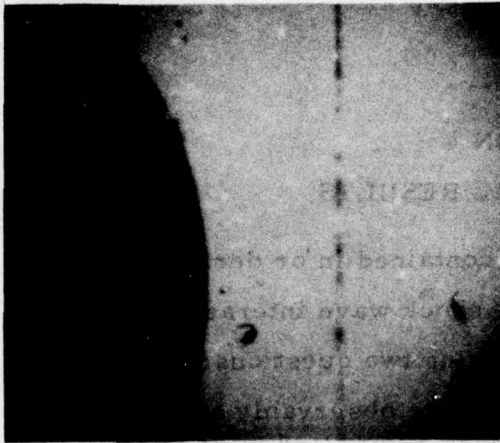
- 1) What size of drops are observably affected while traversing the shock region and what is the nature of that effect?
- 2) What size drops are swept around the projectile without impacting the surface?

#### 4.1 IMAGE CONVERTER PHOTOGRAPHS

A typical image converter photograph sequence is shown in Figure 28 and a series of selected single frames and sequences are contained in Appendix A. The following observations are derived from these photos:

- 1) Resolution is severely limited by phosphor and film grain size and by the maximum magnification achievable (9:1). Small changes in drop shape and/or small drops are not detectable.
- 2) Large drops (100-200  $\mu\text{m}$ ) are clearly shown traversing the bow shock and impacting the surface.
- 3) Impact debris plumes are clearly evident.
- 4) Significant deformation or stripping of the drops was not observed. However, small drops and/or small deformations could not be resolved and question (1) remained unanswered.
- 5) A sweeping of drops around the projectile was not observed and it can be concluded that no significant sweeping occurs for the sizes observed (100-200  $\mu\text{m}$  diameter).





Shot no. 3477

Water drop diameter: 209  $\mu\text{m}$

Velocity: 4119 m/s

Projectile: 10 mm nose radius  
lexan

Range Pressure: 381 Torr

Figure 28. Image converter camera sequence.

## 4.2 MICROSCOPE CAMERA PHOTOGRAPHS

The development of the microscope camera extended resolution down to less than  $5\text{ }\mu\text{m}$  making the observation of small drops and the detection of small droplet deformations and/or mass loss possible. Data was collected down to drop diameters of approximately  $20\text{ }\mu\text{m}$ , the limit of the drop generating system. Below diameters of  $80 - 100\text{ }\mu\text{m}$ , drop generator behavior was erratic and it was difficult to obtain well controlled drop sizes or single streams. These problems compound the difficulty of using the data but a number of pertinent qualitative observations can be made. Data was collected in two velocity regions; high velocity ( $\sim 4\text{ km/s}$ ) and low velocity ( $\sim 1\text{ km/s}$ ).

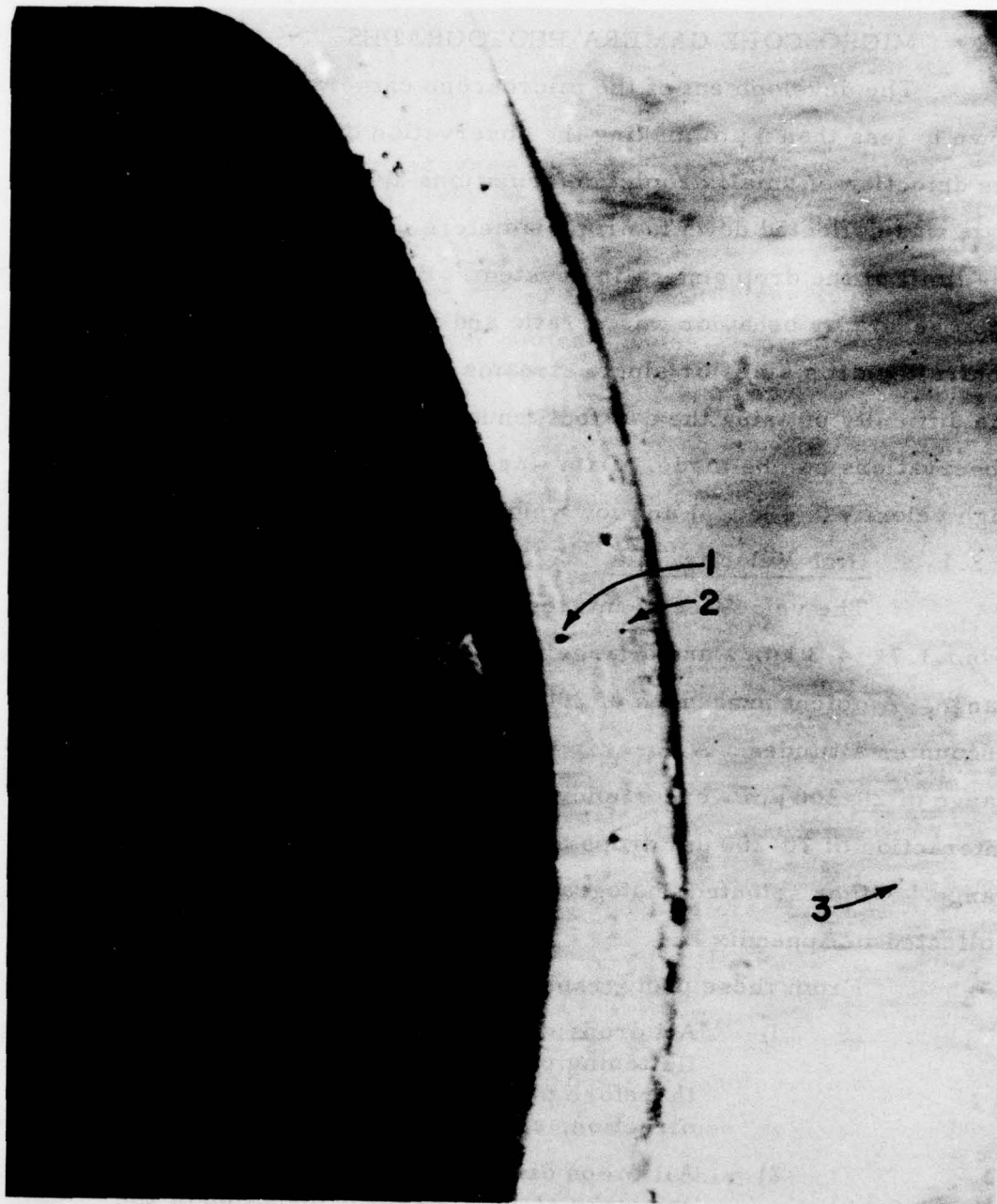
### 4.2.1 High Velocity Data

The velocities of interest in high velocity rain erosion are from  $3.7 - 4.3\text{ km/s}$  and a large number of shots were fired in this range. Ambient pressures of 300-500 Torr were used to simulate encounter altitudes. A nose tip radius of 1 cm and drops in the diameter range of  $20-200\text{ }\mu\text{m}$  were employed. Figures 29 and 30 show the interaction of  $70-200\text{ }\mu\text{m}$  drops and Figure 31 shows drops in  $15-80\text{ }\mu\text{m}$  range. Other selected photographs of high velocity encounters are collected in Appendix B.

From these photographs the following observations are made:

- 1) All drops within the shock region display a flattening parallel to the shock front and therefore perpendicular to the gas flow direction, as might be expected.
- 2) All drops display well developed bow shocks and wake structures. Perturbation of the projectile bow shock is clearly evident.
- 3) No significant mass stripping is evident and even very small drops ( $>15\text{ }\mu\text{m}$ ) arrive near the surface, deformed but apparently intact (Figure 31). The undeformed size of observed drops inside the shock region is at present not possible to determine, so the original size of small drops near the projectile is open to question.





Shot. no. 3577

Water drop diameter:

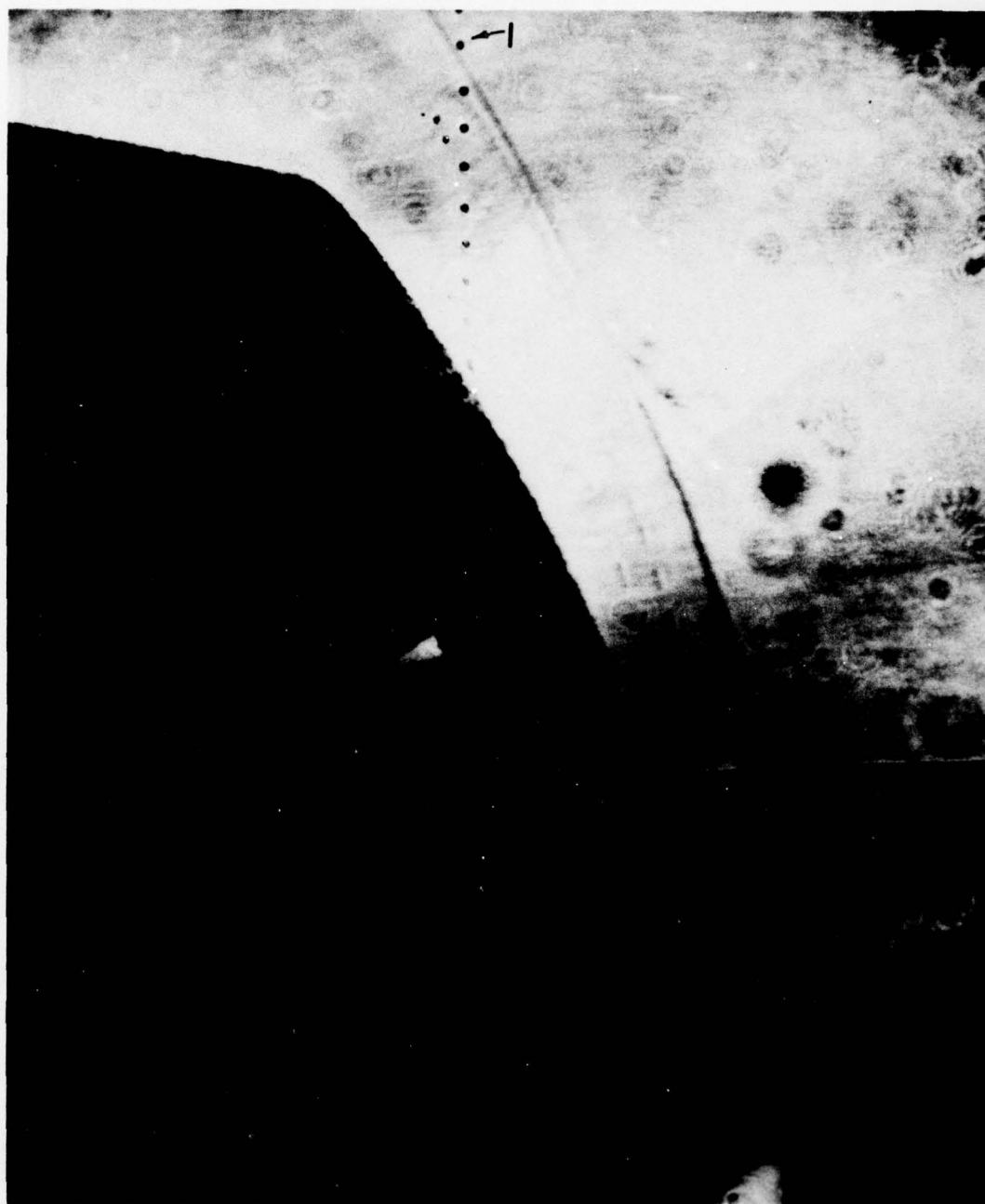
- 1) 74  $\mu\text{m}$
- 2) 40  $\mu\text{m}$
- 3) 10  $\mu\text{m}$

Projectile: 12.7 mm nose  
radius lexan

Velocity: 3.5 km/s

Range Pressure: 508 Torr

Figure 29. Microscope/laser camera picture.

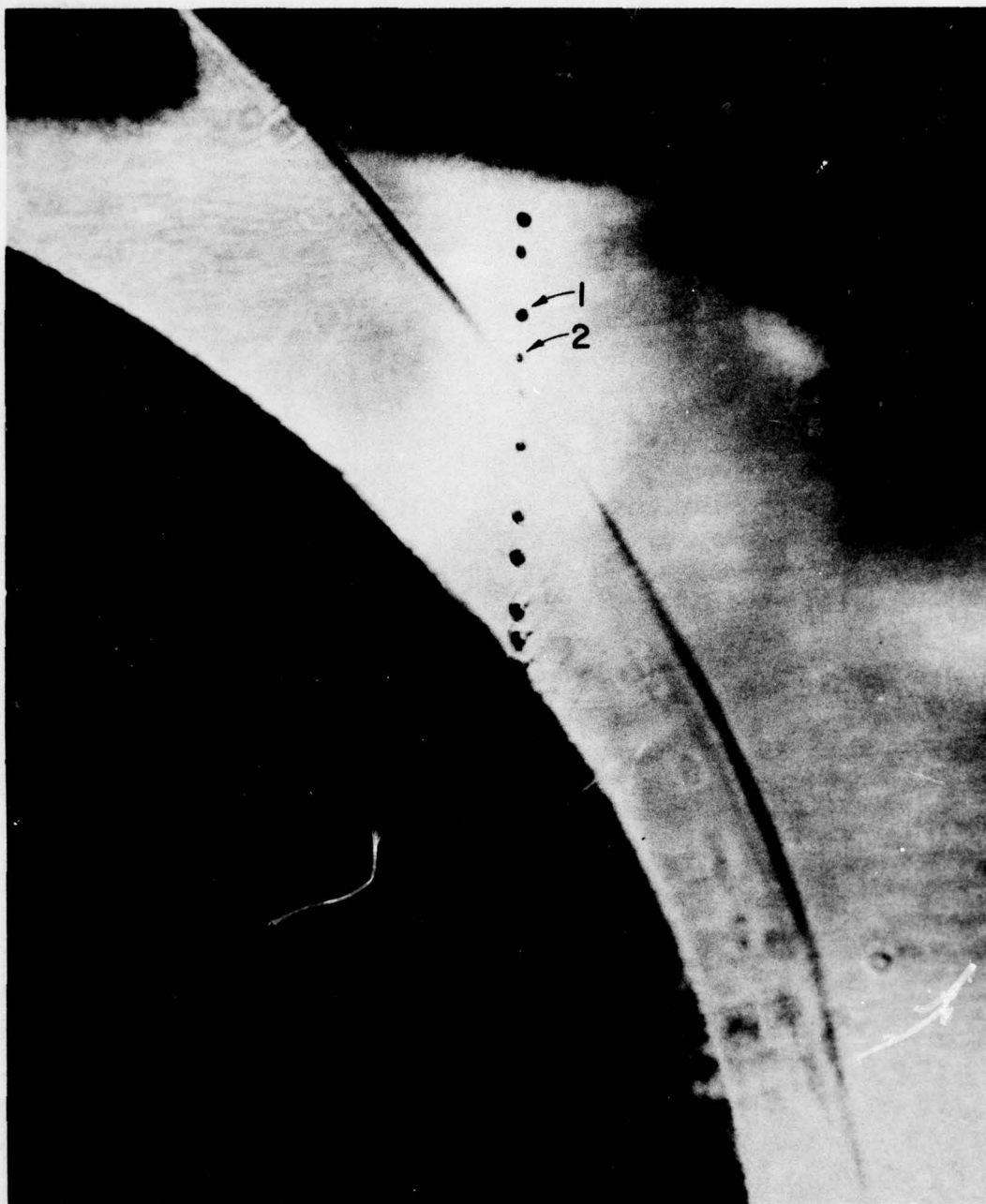


Shot no. 3604

Water drop diameter:	Projectile: 12.7 mm nose
1) 86 $\mu\text{m}$	radius lexan
	Velocity: 3.6 km/s
	Range Pressure: 381 Torr

Figure 30. Microscope/laser camera picture.





Shot no. 3583

Water drop diameter:

1) 126  $\mu\text{m}$

2) 90  $\mu\text{m}$

Projectile: 12.7 mm nose  
radius lexan

Velocity: 4.2 km/s

Range Pressure: 508 Torr

Figure 31. Microscope/laser camera picture.

However, as significant mass stripping is not evident, the apparent size with due account taken for deformation is probably a good estimate of original size.\*

- 4) Catastrophic failure of drops is not observed although the lenticular shapes and "parachutes" present in Figure 31 could well be debris remaining from the disintegration of very small drops. They could also be shock front disruption due to droplet penetration "over the horizon."
- 5) No significant sweeping action is observed for even the smallest drops observed near the corner of the projectile nose, where radial flow should be relatively high.

#### 4.2.2 Low Velocity Data

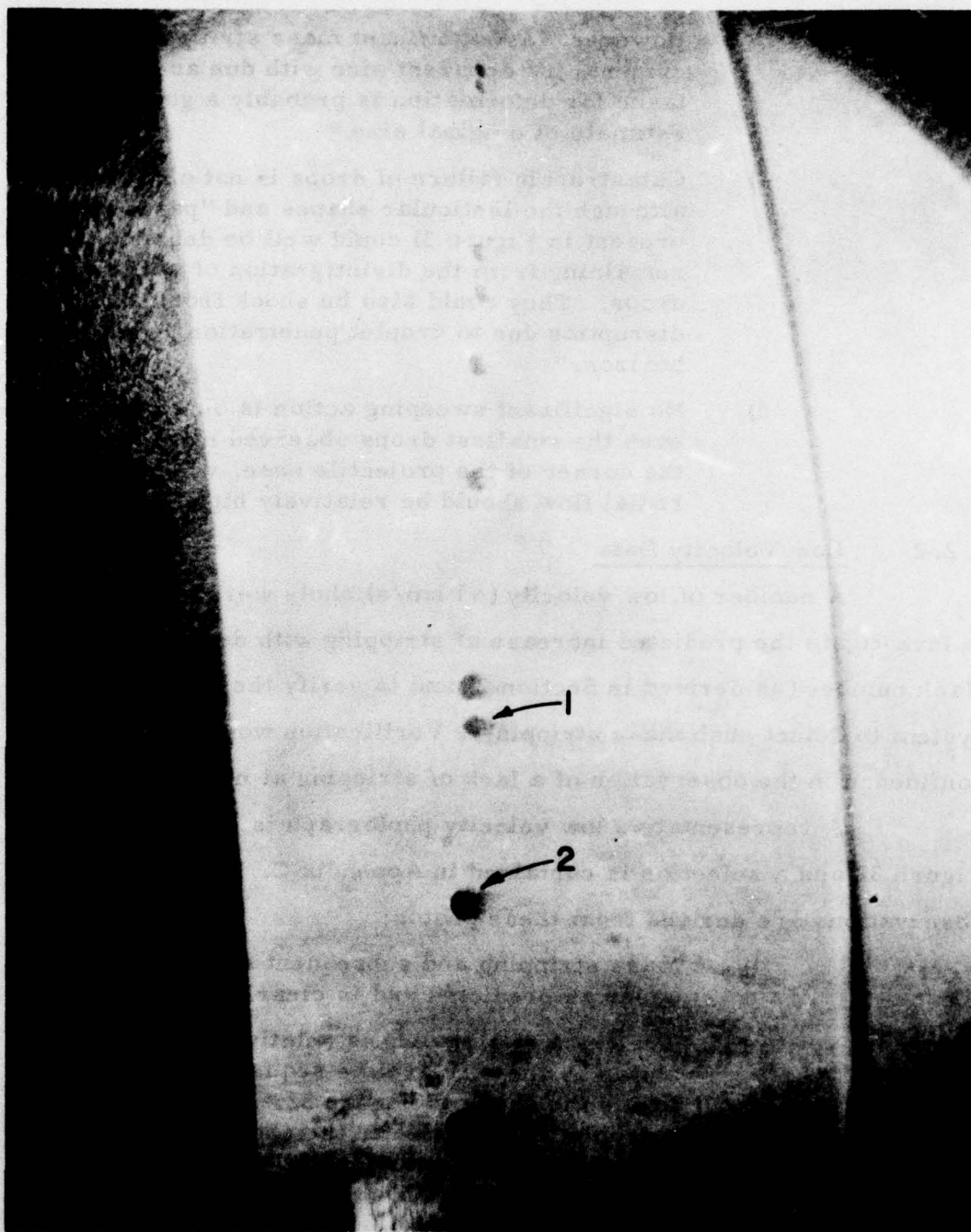
A number of low velocity ( $\sim 1$  km/s) shots were made to investigate the predicted increase of stripping with decreasing Mach number (as derived in Section 3) and to verify the ability of the system to detect such mass stripping. Verification would increase confidence in the observation of a lack of stripping at high velocity.

A representative low velocity photograph is shown in Figure 32 and a selection is contained in Appendix C. The following observations are derived from these photos:

- 1) Mass stripping and subsequent streaming does occur as predicted and is clearly detectable.
- 2) The onset of stripping is relatively abrupt as shown by the virtual time sequence of drops inside the shock in Figure 32. The time that a droplet has resided in the shock region is approximately proportional to its horizontal distance from the shock front.
- 3) Significant mass persists and impacts the projectile for the size of drops observed ( $>100 \mu\text{m}$ ). (Appendix B, Shot 3529.)

\*After preparation of this report began a photographic system was developed to photograph the droplet field before impact. This provides a reliable measure of the unaffected drop size.





Shot no. 3533

Water drop diameter:

1) 134  $\mu\text{m}$

2) 222  $\mu\text{m}$

Projectile: flat nose lexan

Velocity: 1.1 km/s

Range Pressure: 508 Torr

Figure 32. Microscope/laser camera picture.

- 4) **Sweeping of drops around the projectile is not observed.**

## SECTION 2 CONCLUSIONS

The analytic study predicted that drop distribution should increase with decreasing Mach number. This was verified experimentally, with the mass stripping of large drops was observed at high velocity (4 km/s) the gross mass stripping and drop distribution was constant at low velocity (1 km/s).

The analytic study predicts that complete disintegration will not occur at 4 km/s for drops above 10-20  $\mu$ m diameter and negligible disintegration was observed for drops of this size. As drops below 10-20  $\mu$ m were unavailable from the existing drop generator, the analysis could not be tested more thoroughly.

No drops were observed to be swept around the nose of the projectile and it is concluded that for the sizes observed no such sweeping occurs.



## SECTION 5

### CONCLUSIONS

The analytic study predicted that drop disruption should increase with decreasing Mach number. This was verified experimentally; very little mass stripping of large drops was observed at high velocity (4 km/s) but gross mass stripping and drop disintegration was observed at low velocity (1 km/s).

The analytic study predicts that complete disintegration will not occur at 4 km/s for drops above 10-20  $\mu\text{m}$  diameter and negligible disintegration was observed for drops of this size. As drops below 10-20  $\mu\text{m}$  were unavailable from the existing drop generator, the analysis could not be tested more thoroughly.

No drops were observed to be swept around the nose of the projectile and it is concluded that for the sizes observed no such sweeping occurs.

# REFERENCE LIST

1. Engle, O. G., "Fragmentation of Waterdrops in the Zone Behind an Air Shock," J. of Res. Nat. Bureau of Stds. 60:245-280, 1958.
2. Ranger, A. A. and Nichols, J. A., "Aerodynamic Shattering of Liquid Droplets," A. I. A. A. J. 7:285-290, 1969.
3. Reinecke, W. G. and McKay, W. L., "Experiments on Waterdrop Breakup Behind Mach 3 to Mach 12 Shocks," Sandia Corporation Res. Rpt. Sc-CR-70-6063.
4. Reinecke, W. G. and Waldman, G. D., "A Study of Drop Breakup Behind Strong Shocks with Application to Flight." AVCO-0110-70-RK, SAMSO-TR-70-42, 1970.
5. Ranger, A. A. and Nichols, J. A., "Atomization of Liquid Droplets in a Convective Gas Stream," Int. J. of Heat and Mass Transfer, 15:1203-1211, 1972.
6. Waldman, G. D., Reinecke, W. G. and Glenn, D. C., "Raindrop Breakup in the Shock Layer of a High-Speed Vehicle," A. I. A. A. J., 10:1200-1204, 1972.
7. Debord, E. K. and Fox, G. E., "The Breakup of Liquid Droplet Columns by Shock Waves," Astronautics Acta., 17, 669-675, 1972.
8. Fox, G. E. and Debora, E. K., "Breakup of Liquid Drops Due to Convective Flow in Shocked Sprays," Fourteenth Symposium (International) on Combustion, University Park, Penn., pg 1365-1373, August 1973.
9. Lewis, C. H., and Burgess, III, E. G., "Charts of Normal Shock Wave Properties in Imperfect Air," Arnold Engineering Development Center report AEDC-TDR-64-43, 1964.
10. Inouye, M., "Shock Standoff Distance for Equilibrium Flow Around Hemispheres Obtained from Numerical Calculations," A. I. A. A. J., 3: 172, 1965.
11. Chu, C. W. and Powers, S. A., "The Calculation of Three-Dimensional Supersonic Flows Around Spherically Capped Smooth Bodies and Wings - Volume 1." Prepared for Air Force Flight Dynamics Laboratory by Northrop Corporation, AD-763-695, Sept., 1972.



12. Chu, C. W. and Powers, S. A., "The Calculation of Three Dimensional Supersonic Flows Around Spherically-Capped Smooth Bodies and Wings," Prepared for Air Force Flight Dynamics Laboratory by Northrop Corporation, AD-753-696, 1972.
13. Rose, P. H. and Stark, W. L., "Stagnation Point Heat-Transfer Measurement in Dissociated Air," J. of Aero. Sci., 25:86-97, 1958.
14. Lees, L., "Laminar Heat Transfer Over Blunt-Nosed Bodies at Hypersonic Flight Speeds," Jet Propulsion, 26:259-269, 1956.
15. Halperson, S., Boltz, P. T. and Hall, D. A., "High-Velocity-Projectile Drag Determination," 4th Hypervelocity Impact Symposium, Vol. III., Denver.
16. Preonas, D. D. and Swift, H. F., "A High Intensity Point Light Source," 9th International Congress on High Speed Photography, Denver, August, 1970.

**APPENDIX A**

**IMAGE CONVERTER CAMERA SYSTEM PHOTOGRAPHS**





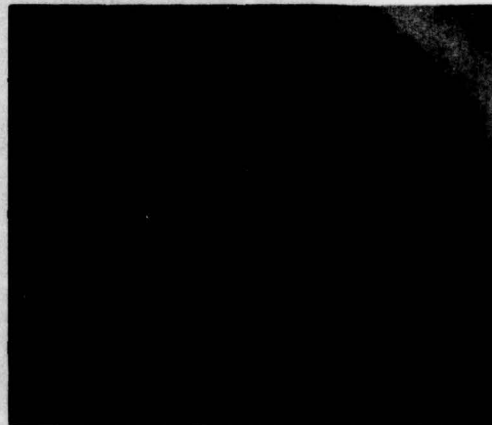
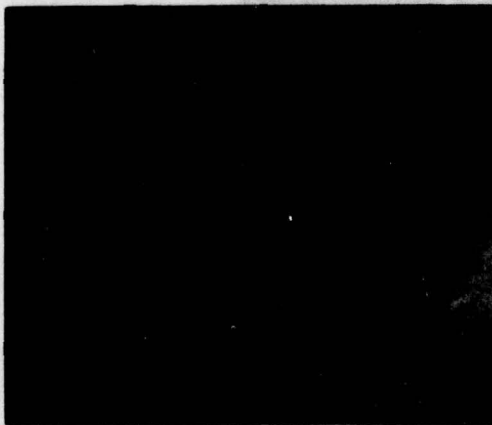
Shot no. 3416  
Water drop size: 369  $\mu\text{m}$       Velocity: 5026 m/s  
Projectile: Flat nose lexan      Range Pressure: 140 Torr



Shot no. 3433

Water drop size: 266  $\mu\text{m}$   
Projectile: Flat nose lexan

Velocity: 4614 m/s  
Range Pressure: 140 Torr

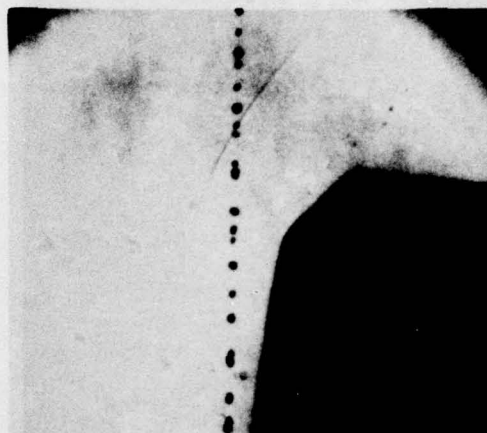
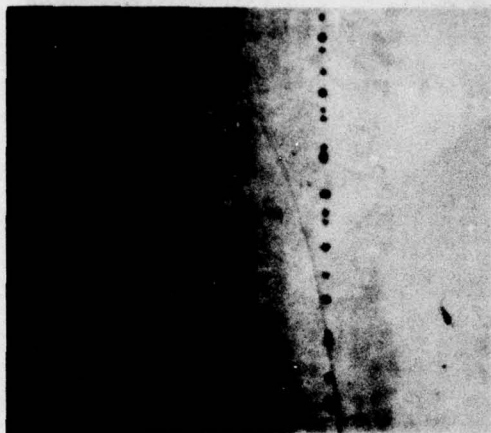


Shot no. 3439

Water drop size: 221  $\mu\text{m}$   
Projectile: 6.5 mm nose radius  
lexan

Velocity 4741 m/s  
Range Pressure: 140 Torr





Shot no. 3456

Water drop size: 164  $\mu\text{m}$   
 Projectile: Flat nose lexan

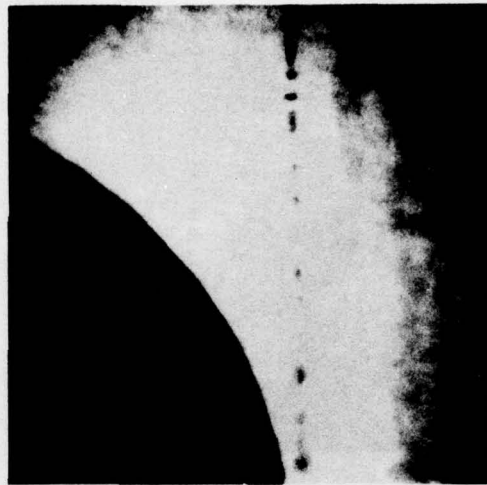
Velocity: 4451 m/s  
 Range Pressure: 140 Torr



Shot no. 3460

Water drop size: 205  $\mu\text{m}$   
 Projectile: 10 mm nose radius  
 lexan

Velocity: 4197 m/s  
 Range Pressure: 140 Torr

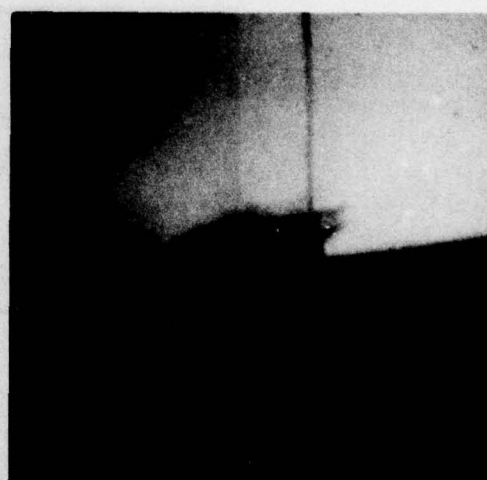
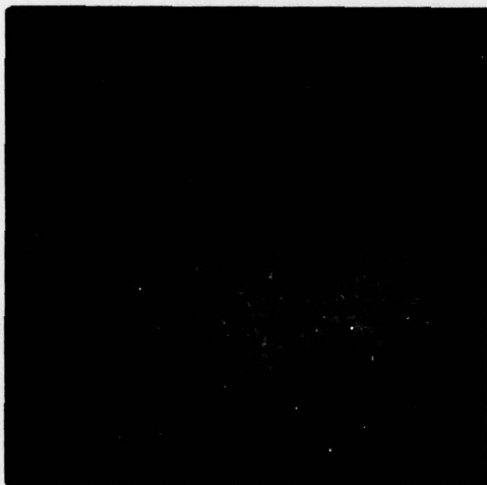


Shot no. 3465

Water drop size: 207  $\mu\text{m}$   
 Projectile: 10 mm nose radius  
 lexan

Velocity: 4258 m/s  
 Range Pressure: 140 Torr





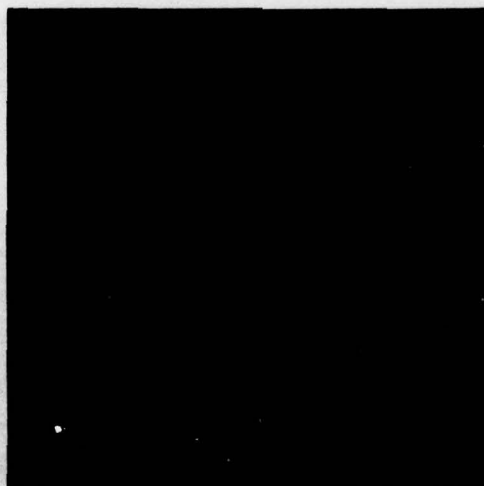
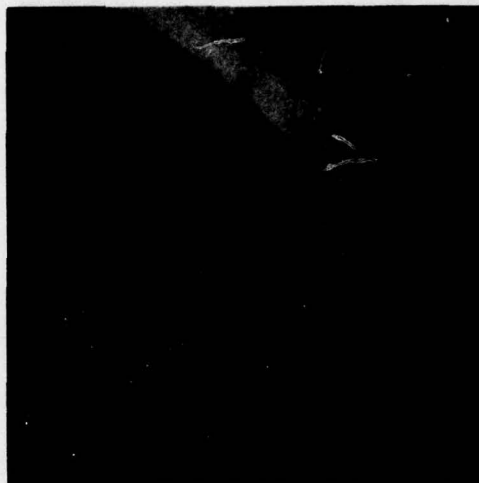
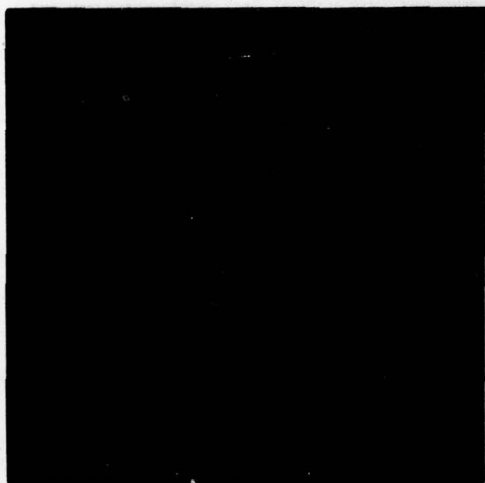
Shot no. 3466

Water drop size: 250  $\mu\text{m}$

Velocity: 4156 m/s

Projectile: 10 mm nose radius  
lexan

Range Pressure: 140 Torr



Shot no. 3501

Water drop size: 209  $\mu\text{m}$

Velocity: 5026 m/s

Projectile: 10 mm nose radius  
lexan

Range Pressure: 508 Torr

**APPENDIX B**

**MICROSCOPE/LASER CAMERA SYSTEM PHOTOGRAPHS  
HIGH VELOCITY ENCOUNTERS**





Shot no. 3607

Water drop size: 1) 132  $\mu\text{m}$   
2) 118  $\mu\text{m}$   
3) 55  $\mu\text{m}$

Projectile: 12.7 mm nose  
radius lexan  
Velocity: 3.5 km/s  
Range Pressure: 381 Torr



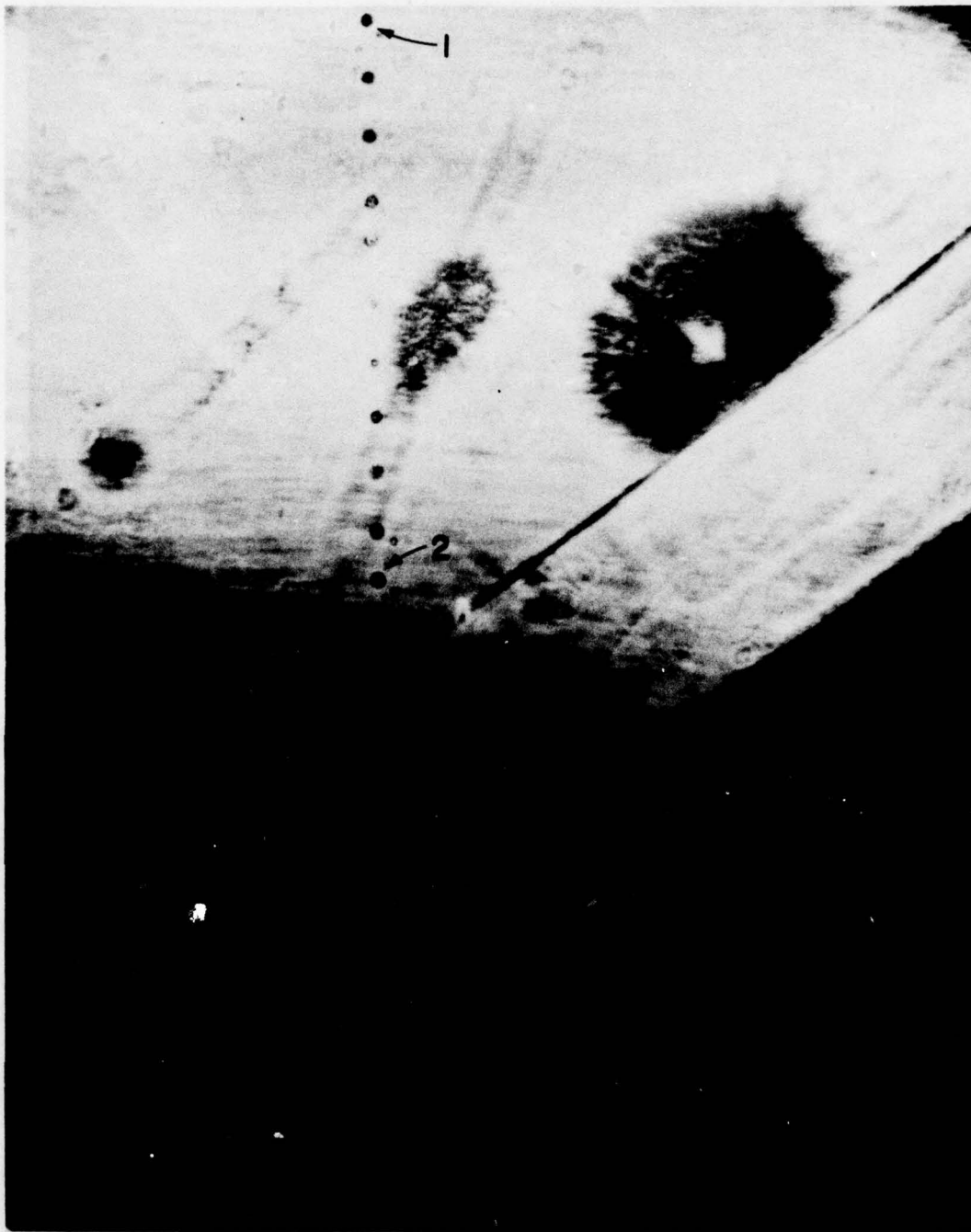
Shot no. 3606

Water drop size: 1) 82  $\mu\text{m}$   
2) 73  $\mu\text{m}$

Projectile: 12.7 mm nose  
radius lexan

Velocity: 3.7 km/s

Range Pressure: 381 Torr



Shot no. 3608

Water drop size: 1) 115  $\mu\text{m}$   
2) 147  $\mu\text{m}$

Projectile: 12.7 mm nose  
radius lexan

Velocity: 4.3 km/s

Range Pressure: 381 Torr





Shot no. 3573

Water drop size: 1) 27  $\mu\text{m}$   
2) 36  $\mu\text{m}$   
3) 24  $\mu\text{m}$

Projectile: 10 mm nose  
radius lexan

Velocity: 3.5 km/s

Range Pressure: 381 Torr

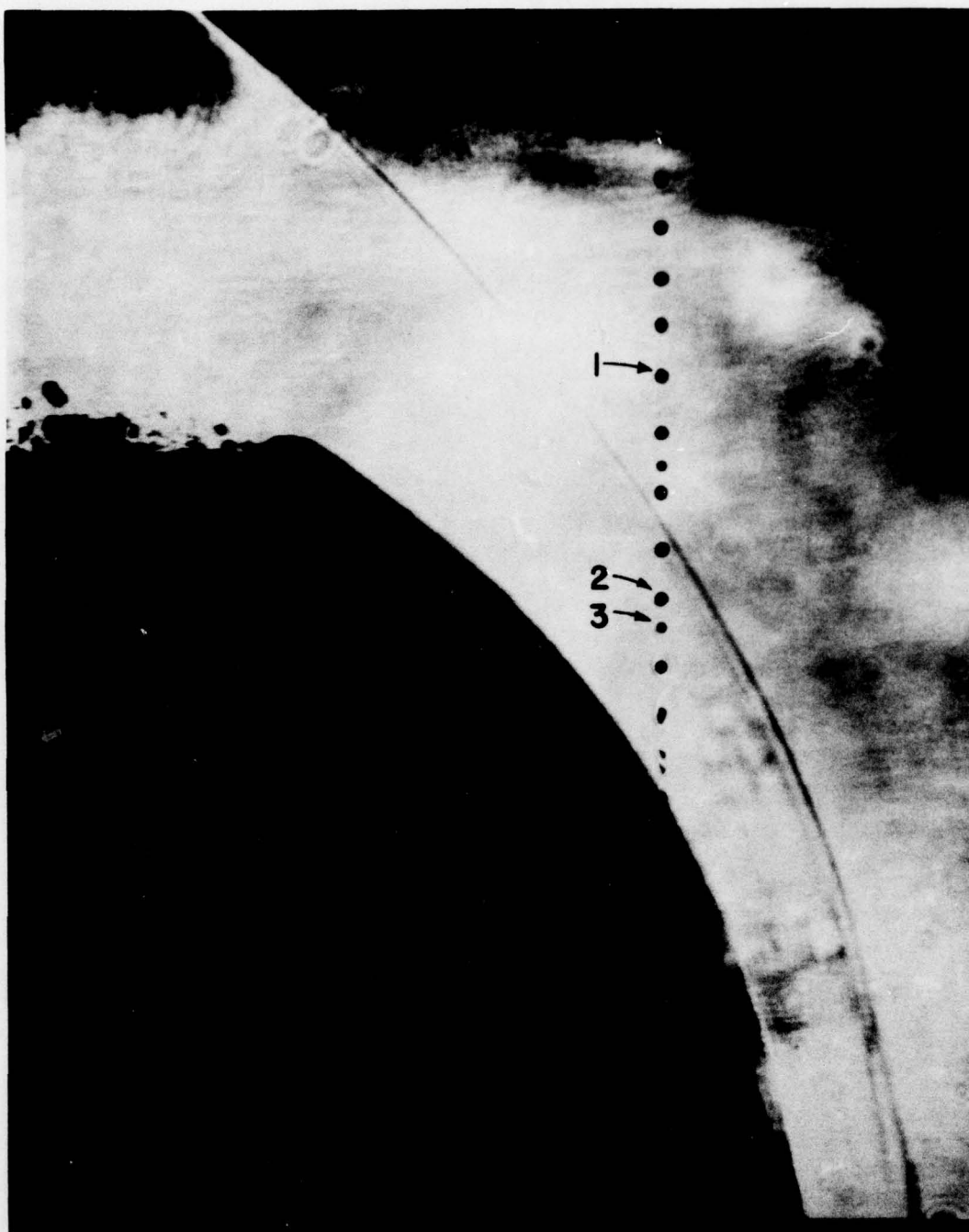


Shot no. 3567

Water drop size: 1) 44  $\mu\text{m}$   
2) 39  $\mu\text{m}$   
3) 28  $\mu\text{m}$

Projectile: 10 mm nose  
radius lexan  
Velocity: 3.1 km/s  
Range Pressure: 508 Torr

B-5



Shot no. 3585

Water drop size: 1) 135  $\mu\text{m}$   
2) 128  $\mu\text{m}$   
3) 97  $\mu\text{m}$

Projectile: 10 mm graphite  
nose radius lexan

Velocity: 2.9 km/s

Range Pressure: 381 Torr





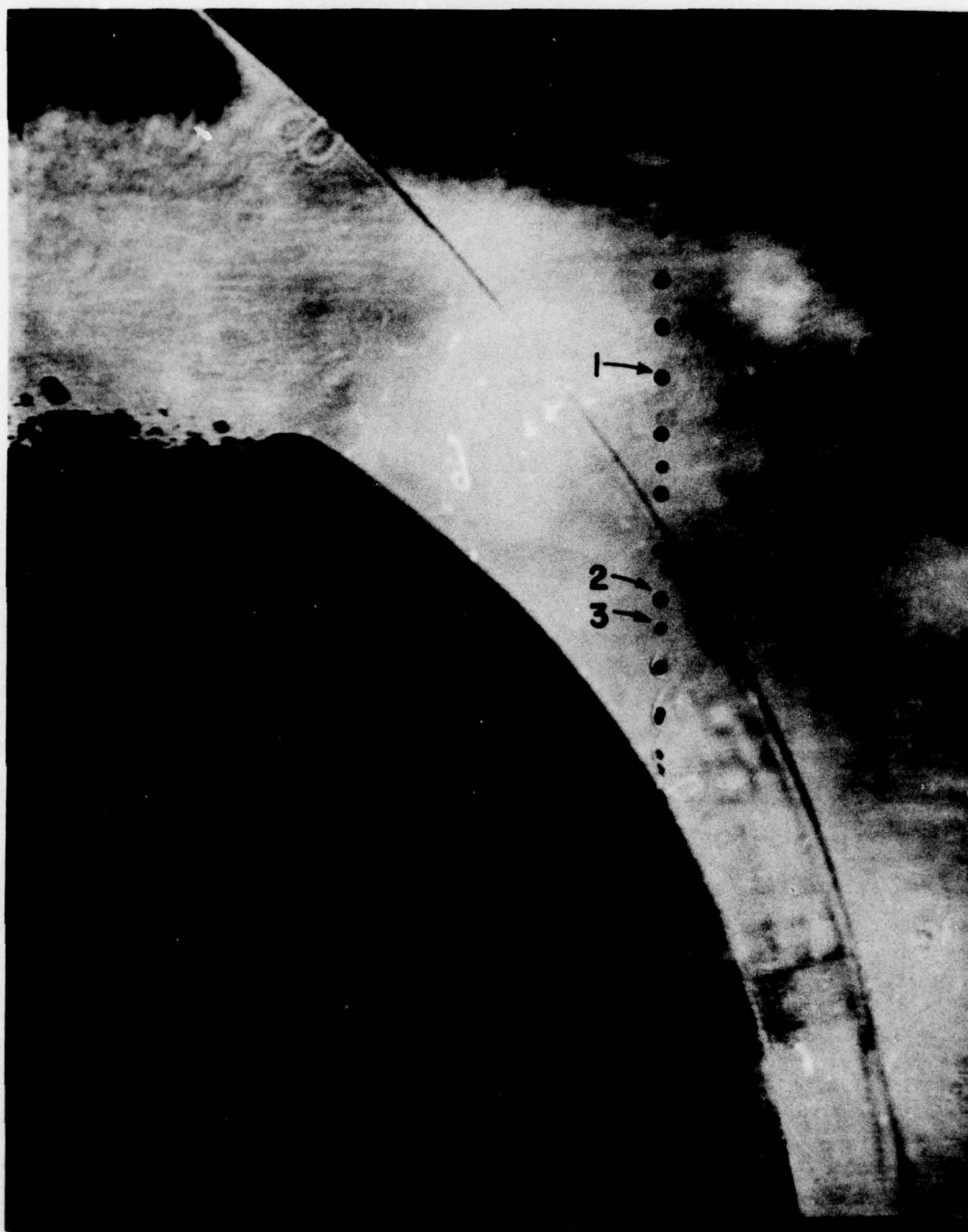
Shot no 3603

Water drop size: 1) 77  $\mu\text{m}$   
2) 73  $\mu\text{m}$

Projectile: 12.7 mm nose  
radius lexan

Velocity: 3.5 km/s

Range Pressure: 381 Torr



Shot no. 3585

Water drop size: 1) 135  $\mu\text{m}$   
2) 128  $\mu\text{m}$   
3) 97  $\mu\text{m}$

Projectile: 10 mm graphite  
nose radius lexan  
Velocity: 2.9 km/s  
Range Pressure: 381 Torr



Shot no. 3604

Water drop diameter:

1) 86  $\mu\text{m}$

Projectile: 12.7 mm nose  
radius lexan

Velocity: 3.6 km/s

Range Pressure: 381 Torr





Shot no. 3603

Water drop size: 1) 77  $\mu\text{m}$   
2) 73  $\mu\text{m}$

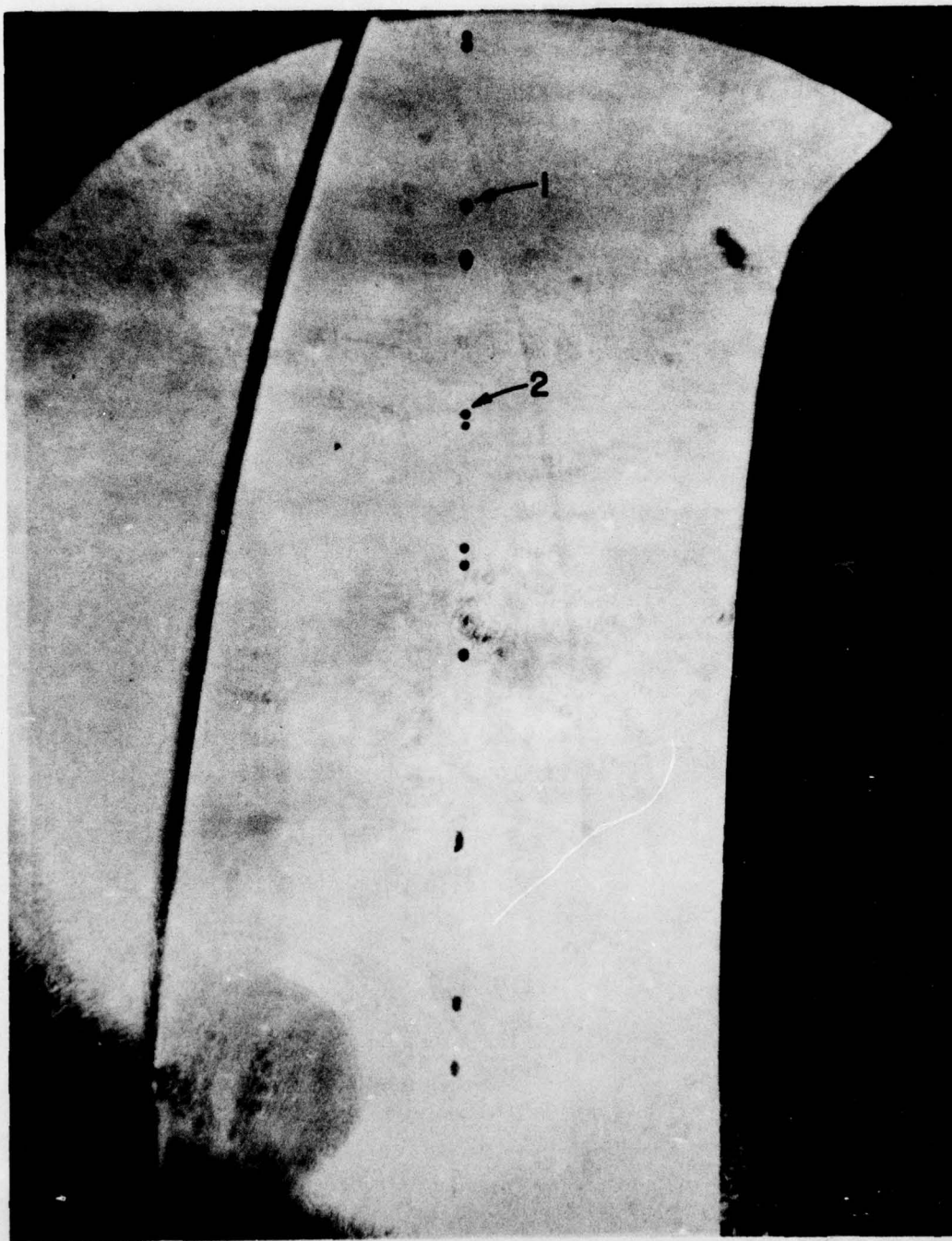
Projectile: 12.7 mm nose  
radius lexan

Velocity: 3.5 km/s

Range Pressure: 381 Torr

**APPENDIX C**

**MICROSCOPE/LASER CAMERA SYSTEM PHOTOGRAPHS  
LOW VELOCITY ENCOUNTERS**



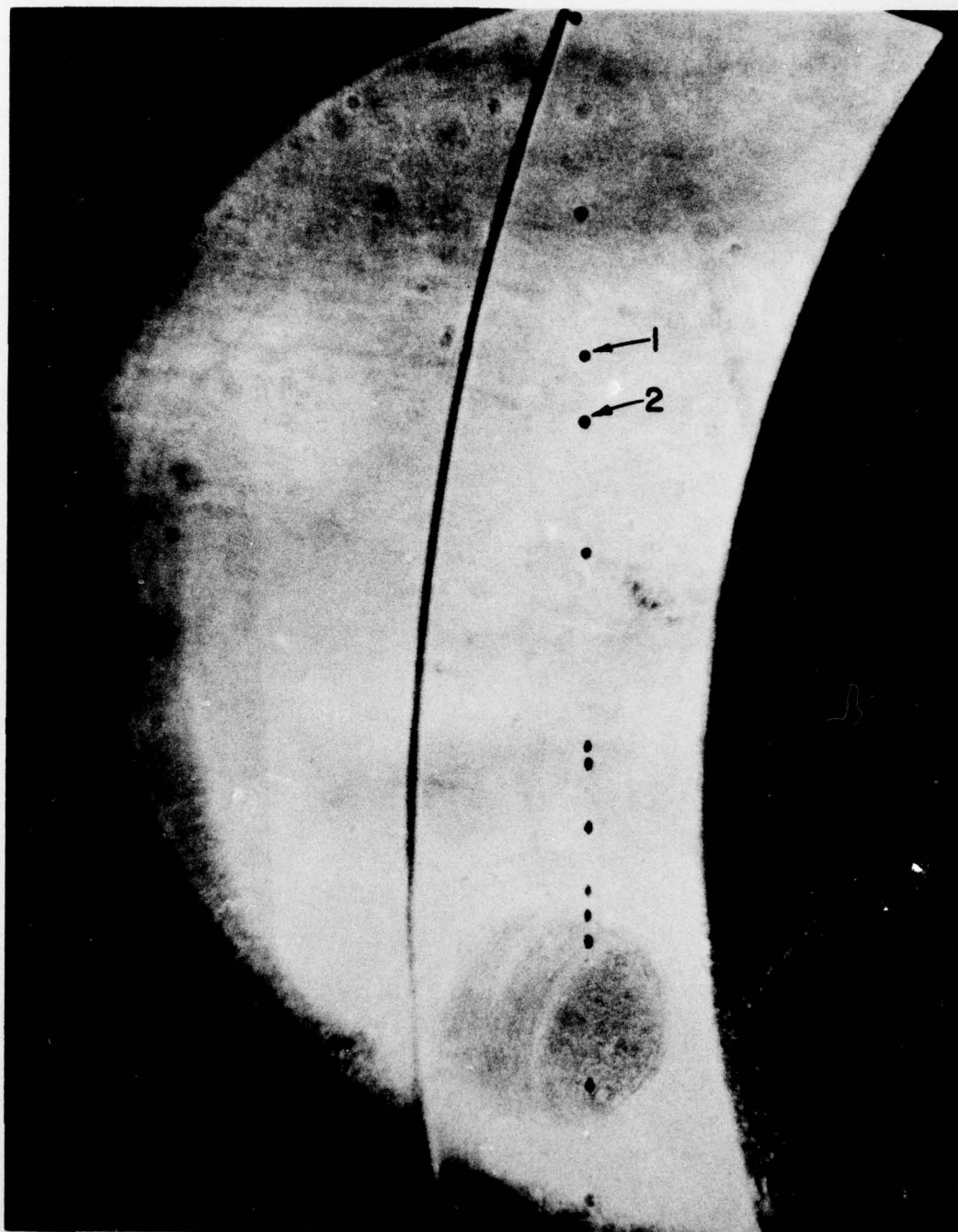
Shot no. 3530

Water drop size: 1) 116  $\mu\text{m}$   
2) 100  $\mu\text{m}$

Projectile: flat nose lexan  
Velocity: 1.1 km/s  
Range Pressure: 508 Torr

C-1





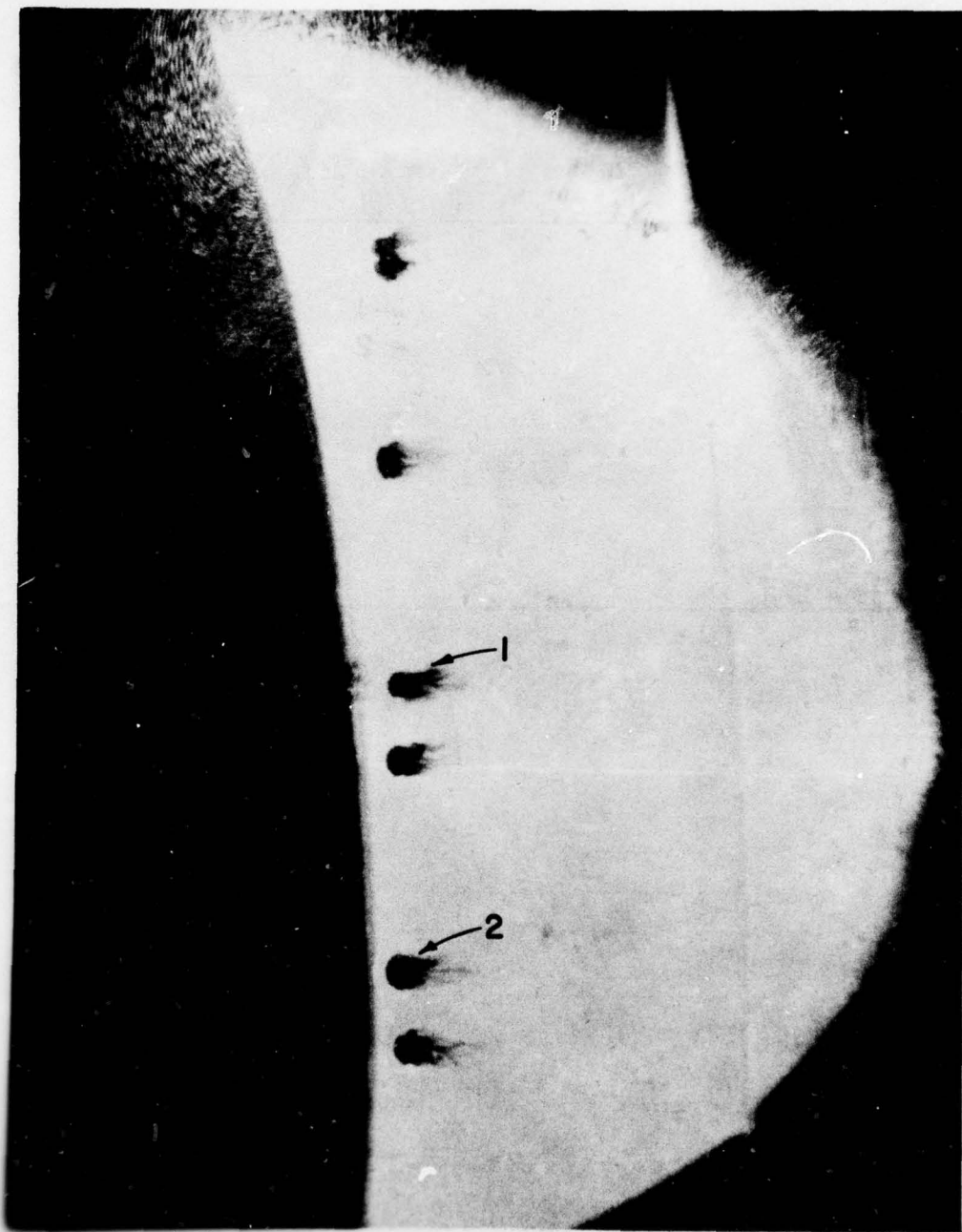
Shot no. 3528

Water drop size: 1)  $101\text{ }\mu\text{m}$   
2)  $117\text{ }\mu\text{m}$

Projectile: 12.7 mm nose  
radius lexan

Velocity: 1.1 km/s

Range Pressure: 508 Torr

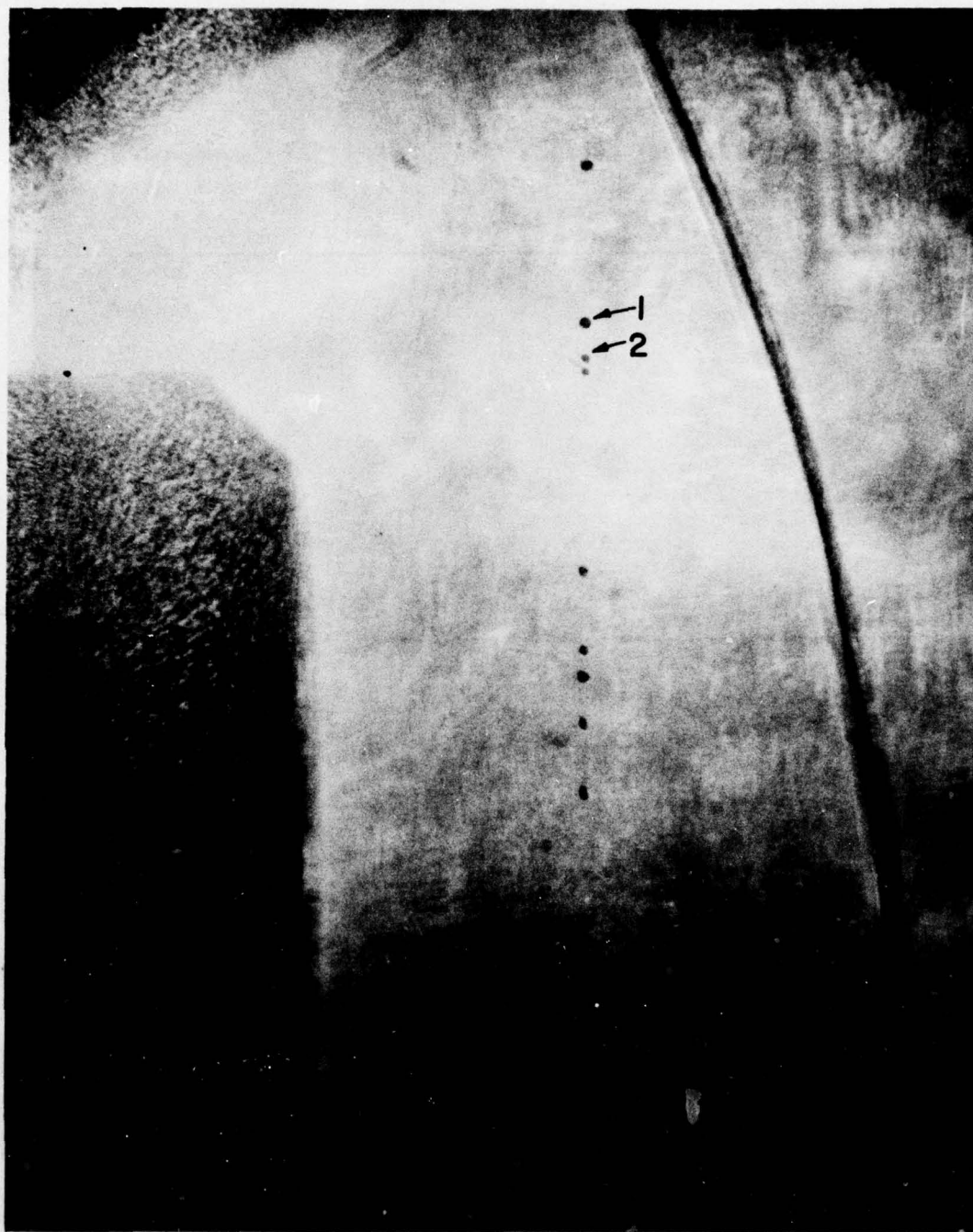


Shot no. 3529

Water drop size: 1) 162  $\mu\text{m}$   
2) 313  $\mu\text{m}$

Projectile: flat nose lexan  
Velocity: 1.1 km/s  
Range Pressure: 508 Torr

C-3

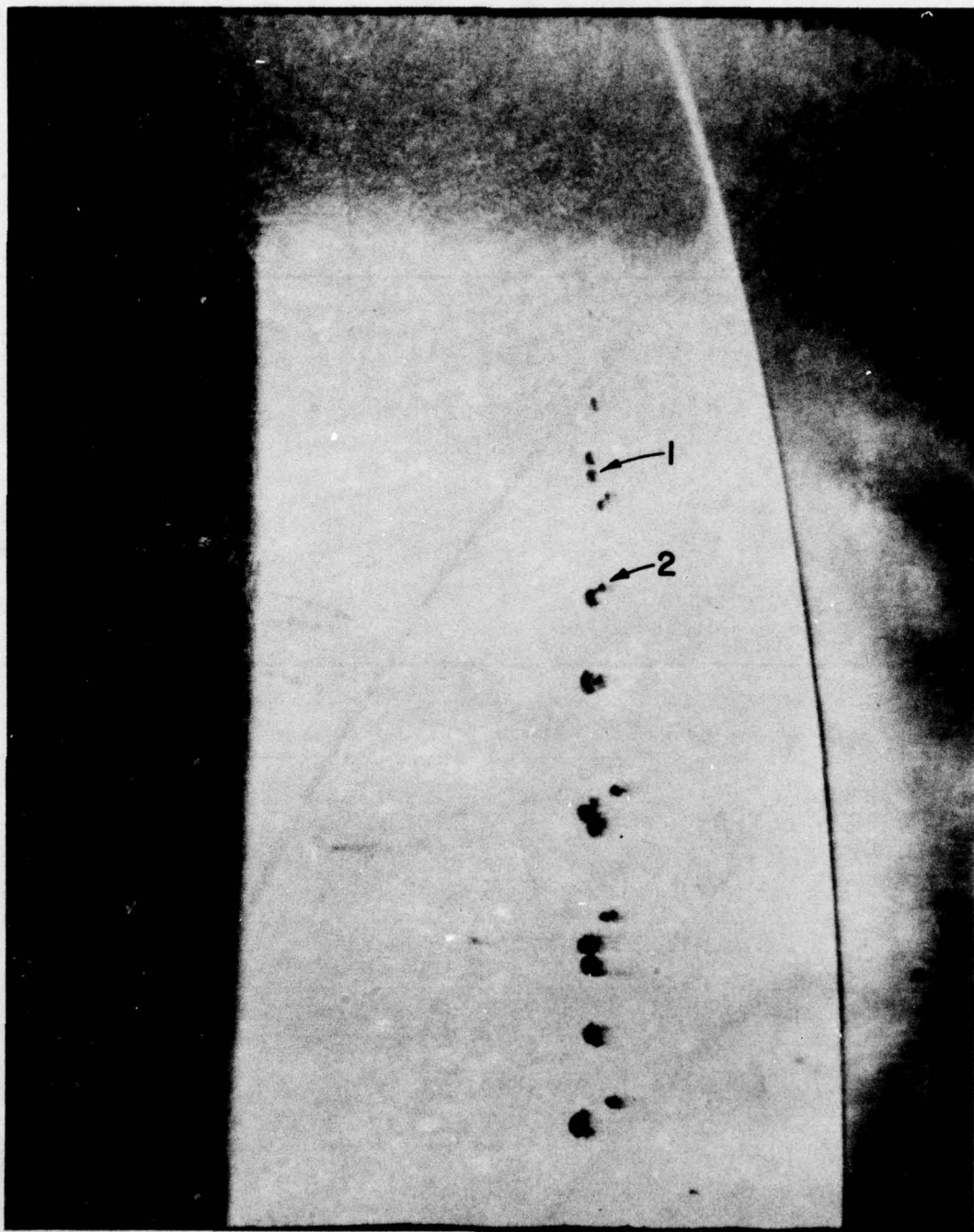


Shot no. 3532

Water drop size: 1) 113  $\mu\text{m}$   
2) 77  $\mu\text{m}$

Projectile: flat nose lexan  
Velocity: 1.1 km/s  
Range Pressure: 508 Torr

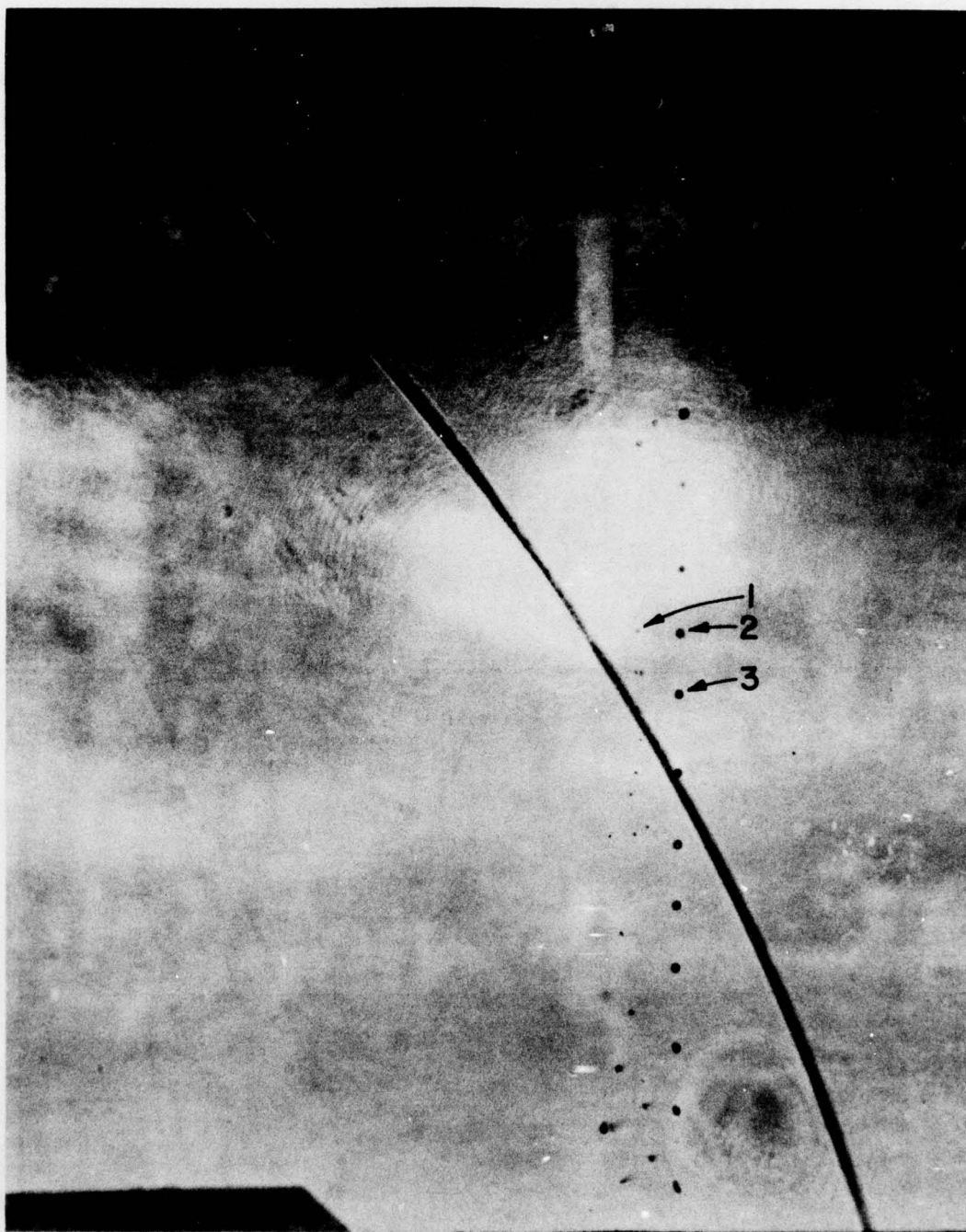




Shot no. 3534

Water drop size: 1) 119  $\mu\text{m}$   
2) 71  $\mu\text{m}$

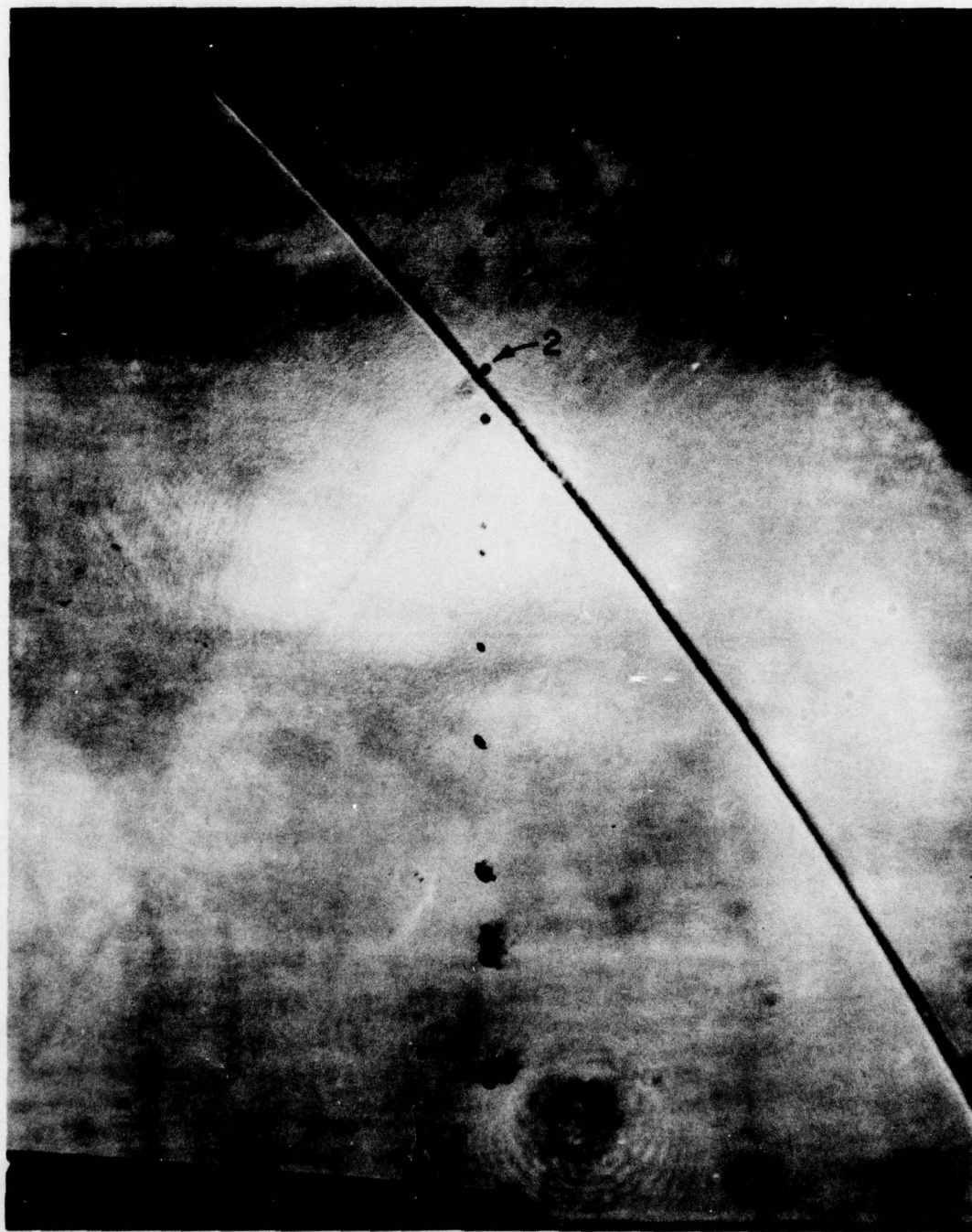
Projectile: flat nose lexan  
Velocity: 1.1 km/s  
Range Pressure: 508 Torr



Shot no. 3537

Water drop size: 1) 26  $\mu\text{m}$   
2) 82  $\mu\text{m}$   
3) 83  $\mu\text{m}$

Projectile: flat nose lexan  
Velocity: 1.1 km/s  
Range Pressure: 508 Torr



Shot no. 3542

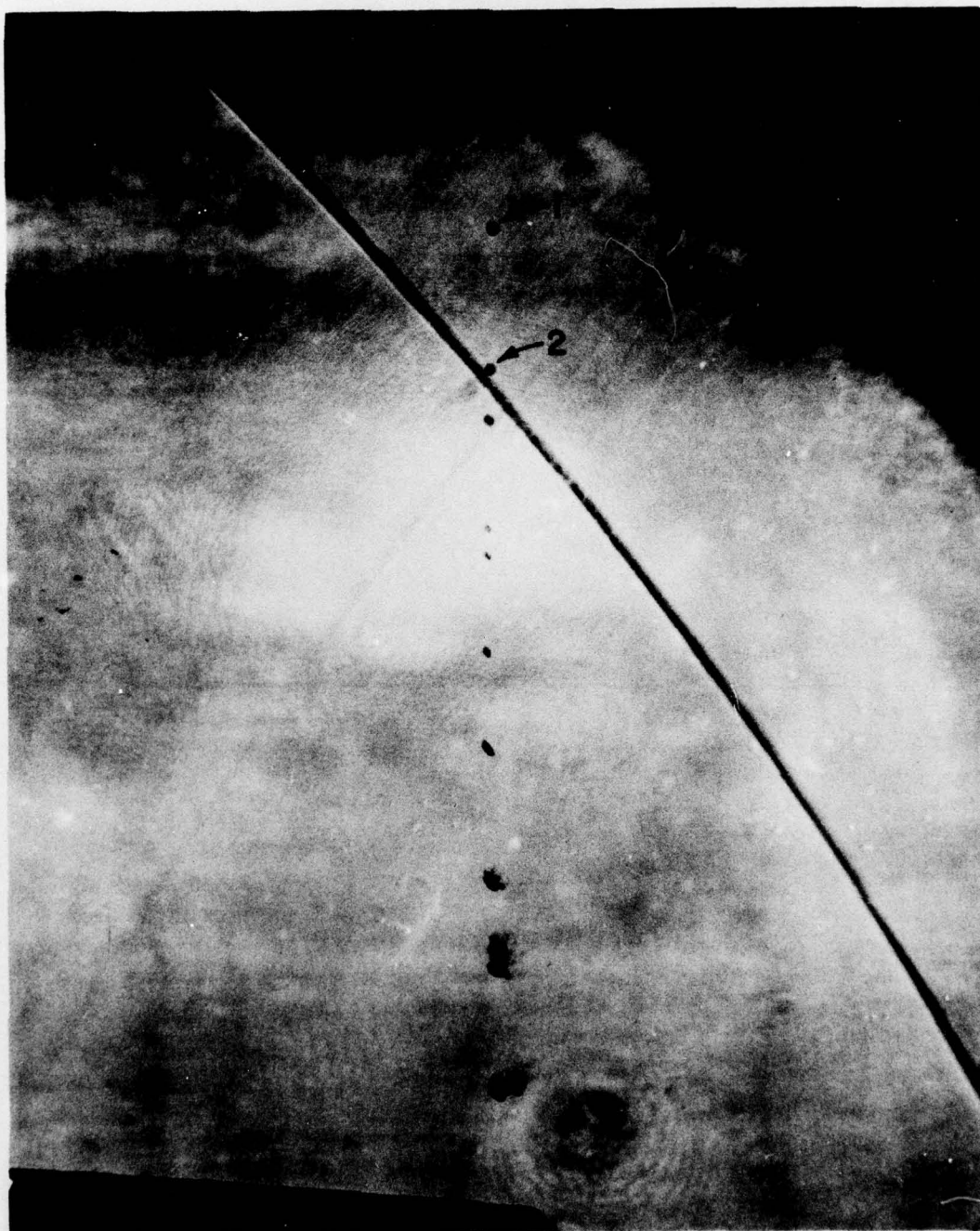
Water drop size: 1) 129  $\mu\text{m}$   
2) 122  $\mu\text{m}$

Projectile: 12.7 mm nose  
radius lexan

Velocity: 1.1 km/s

Range Pressure: 508 Torr





Shot no. 3542

Water drop size: 1) 129  $\mu\text{m}$   
2) 122  $\mu\text{m}$

Projectile: 12.7 mm nose  
radius lexan

Velocity: 1.1 km/s

Range Pressure: 508 Torr

C-8